

# Progress Report on Numerical Modeling of a Prototype Fuel Cell

Otávio Beruski,<sup>1,2,\*</sup> Ivan Korkischko,<sup>1,2</sup> Thiago Lopes,<sup>1,2</sup> and Fabio Coral Fonseca<sup>1,2</sup>

<sup>1</sup>*Instituto de Pesquisas Energéticas e Nucleares,  
IPEN/CNEN-SP, 05508-000, São Paulo, São Paulo, Brazil*

<sup>2</sup>*Research Centre for Gas Innovation,  
University of São Paulo, Escola Politécnica,  
05508-030, São Paulo, São Paulo, Brazil*

## Abstract

Progress on the numerical modeling of a prototype fuel cell is reported. Known limitations of the original model are addressed, such as a diluted approach to species transport and a homogeneous reaction model, in order to better reflect the understanding of the physical processes. A mesh convergence study is carried out on the improved model, and a comparison between model frameworks is made. Non-monotonic behavior is seen for relevant variables in the convergence study, indicating these are not in the asymptotic regime even at the finer meshes available. Error estimates were obtained using extrapolation schemes and a proxy, reduced computational geometry, resulting in average errors of  $\sim 10\%$ . Model comparison shows better correlation between the improved model and available experimental data, however it lacks validation power when the error estimates are taken in account. Further model improvements are envisioned, as well as the necessity for additional experimental data and computational resources for validation.

---

\* oberuski@alumni.usp.br

## I. INTRODUCTION

This work builds on a previously published model of a prototype fuel cell cathode[1], with the main goal of improving the mathematical framework and therefore the model’s accuracy. Known limitations of the original model were addressed, such as the use of Fick’s law for species diffusion and a homogeneous reaction model. In addition, a mesh convergence study was carried out in order to assess the model’s uncertainty due to discretization of the computational domains, and thus provide an estimate of its precision. The remainder of this work is organized as follows. Section II provides an overview of the original model’s mathematical formulation and the improvements made, as well as a description of the mesh convergence study. Section III first presents the observed behavior of relevant variables with mesh resolution, then proceeds to compare the original model to the improved one. Finally, Section IV concludes with a summary of the results and brief remarks on future studies.

## II. METHODS

The model simulates a prototype polymer electrolyte fuel cell (PEFC), a half-cell originally described by Lopes et al.[2], and as such the relevant domains included are: i) the flow channel (Ch), in this case a single serpentine geometry, ii) the porous transport layer, here comprising only a macroporous substrate (MPS) made of carbon paper (representing Toray TGH-060 with a 10% PTFE hydrophobic treatment), and iii) the catalyst layer (CL), where the catalyst and substrate particles are considered homogeneously distributed (representing Sigma Aldrich Nano Silica Gel on TLC plates, see [2] for details). Domains ii) and iii) comprise the porous media domains (Pm). Figure 1 shows the domains’ disposition and Table I presents the geometrical parameters.

The setup used for all simulations was a workstation with two Intel® Xeon® E3 processors and 128GB of RAM, operated with a 64 bits Debian9 distribution, Linux kernel v. 4.9.0-4. The software used was the commercial package COMSOL Multiphysics®, v.5.1.0.234, along with the Batteries and Fuel Cell, CFD, and Chemical Engineering modules. All data handling and processing was done using GNU Octave v.4.2.1[3].

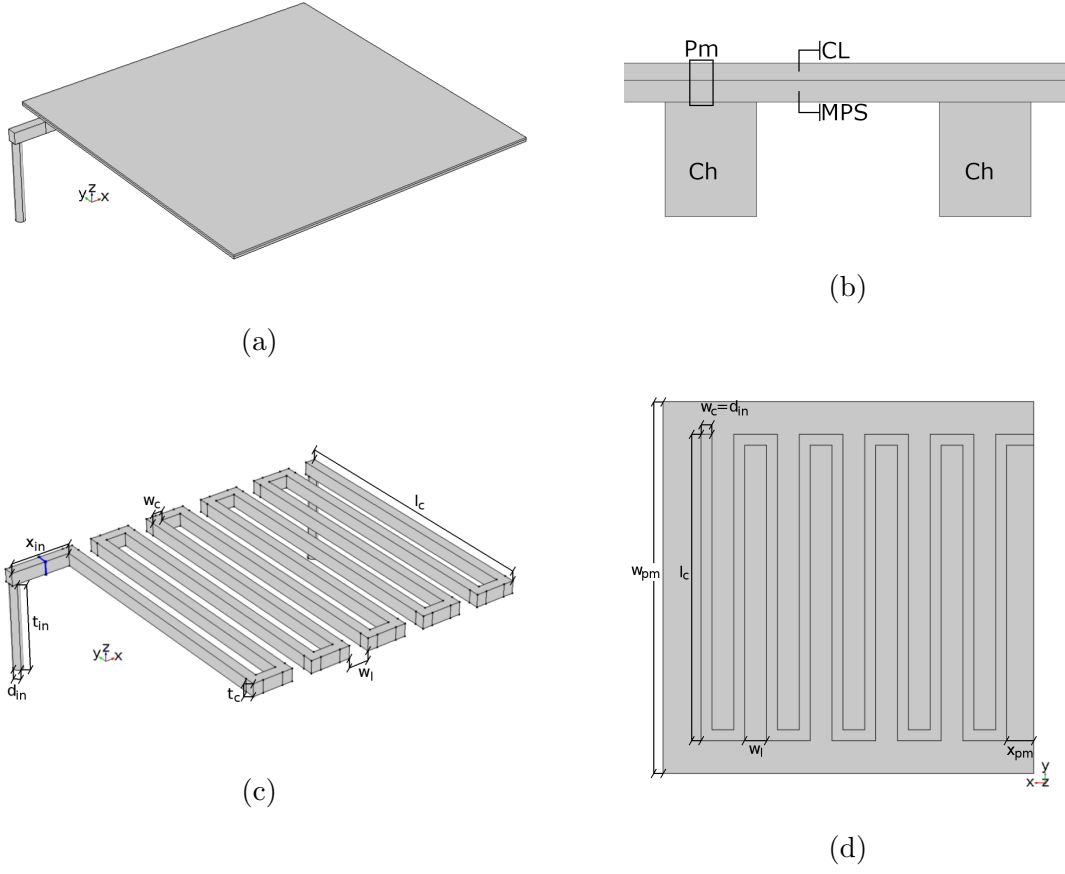


FIG. 1: Geometry used in the proto-cell simulations: **(a)** full geometry, showing the flow channel (Ch) and porous media (Pm) domains; **(b)** cross-section in the  $xz$  plane, showing the structure along the  $z$  axis; **(c)** Ch domain, with the segmentation edges shown in blue (see text), and **(d)** lower boundary of the MPS domain, showing the projection of the Ch domain.

## A. Mathematical Formulation

### 1. Original model

The original mathematical formulation can be found in [1], but a brief description will be given below followed by the improvements made for this work. The model covers momentum and species transport, assumes thermal equilibrium and was solved to steady state.

The momentum transport is described using the (compressible) Darcy-Brinkman formu-

TABLE I: Geometrical parameters of the computational domains.

Parameter	Symbol	Value
Channel width	$w_c$	0.8 mm
Land width	$w_l$	1.6 mm
Channel depth	$t_c$	1.0 mm
Channel section length	$l_c$	22.4 mm
Inlet/outlet diameter	$d_{\text{in}}$	0.8 mm
Inlet/outlet length	$t_{\text{in}}$	7.0 mm
Inlet offset	$x_{\text{in}}$	0.188 in
Porous media edge	$w_{\text{pm}}$	$(l_c + x_{\text{in}})$
Porous media offset	$x_{\text{pm}}$	$(x_{\text{in}} - w_w)/2$
MPS thickness	$t_{\text{MPS}}$	190 $\mu\text{m}$
CL thickness	$t_{\text{CL}}$	150 $\mu\text{m}$

lation (DB), which covers both free and porous media flow[4]:

$$\frac{\rho}{\epsilon} (\mathbf{u} \cdot \nabla) \left( \frac{\mathbf{u}}{\epsilon} \right) = \nabla \left[ -P\mathbf{I} + \frac{\mu}{\epsilon} (\nabla \mathbf{u} + (\nabla \mathbf{u})^T) - \frac{2\mu}{3\epsilon} (\nabla \cdot \mathbf{u}) \mathbf{I} \right] - \frac{\mu}{\kappa} \mathbf{u}, \quad (1)$$

where  $\rho$  and  $\mu$  are the fluid's density and kinematic viscosity, respectively,  $\mathbf{u}$  is the velocity field vector,  $P$  is the relative pressure, and  $\epsilon$  and  $\kappa$  are the domain's porosity and permeability, respectively ( $\epsilon = 1$  and  $\kappa \rightarrow \infty$  for free flow). As shown in [1], DB provides a better description of this system when compared to a Stokes-Darcy approach, i.e. manually coupling the Navier-Stokes equation for the Ch domain and Darcy's law for porous media. The parameters are shown in Table II, chosen in order to describe the materials and conditions used (see [2] for additional information). A normal inflow velocity, as inlet, and a constant pressure boundary conditions, for the outlet, were used.

The species transport was originally modeled using a diluted-species approach, coupling the advection-reaction equation:

$$\nabla \cdot \mathbf{J}_{\text{O}_3} + (\mathbf{u} \cdot \nabla) C_{\text{O}_3} = R_{\text{O}_3}, \quad (2)$$

to Fick's law of diffusion, which defines the molar diffusive flux vector:

$$\mathbf{J}_{\text{O}_3} = -D_{\text{O}_3} \nabla C_{\text{O}_3}, \quad (3)$$

where  $D_{O_3}$  and  $C_{O_3}$  are the diffusion coefficient and the concentration of ozone, respectively. Given the inlet concentration of the species of interest,  $O_3$ , of the order  $10^3$  ppm, such an approach was considered reasonable[1]. The diffusion was corrected for porous media transport:

$$D_{O_3}^{Pm} = f_{Pm} D_{O_3}, \quad (4)$$

where  $f_{Pm} = f_{Pm}(\epsilon, \tau)$ , with  $\tau$  being the medium's tortuosity. A common form for  $f_{Pm}$  is:

$$f_{Pm} = \frac{\epsilon}{\tau}, \quad (5)$$

which might be readily used whenever  $\tau$  is available, as is the case of the MPS domain. Otherwise, a porous medium model might be used, typically with the form  $\tau = \tau(\epsilon)$ . In this case, for the CL domain, the Millington & Quirk model was used[5], as implemented in the software, giving  $\tau = \epsilon^{1/2}$ . The reaction term was defined by a homogeneous first-order reaction:

$$R_{O_3} = -k_{app} C_{O_3}, \quad (6)$$

where the apparent reaction rate constant,  $k_{app}$ , is a free parameter to be adjusted against experimental data. Parameters are shown in Table II.

TABLE II: Parametererization of both models.

Parameter	Symbol	Value	Reference
Reference pressure	$P_{ref}$	1.027 bar	[1]
Cell back pressure	$P_{out}$	$1.0994 \text{ bar} - P_{ref}$	[1]
Carbon paper porosity	$\epsilon_{MPS}$	0.801	[6]
Carbon paper permeability	$\kappa_{MPS}$	$9.18 \times 10^{-12} \text{ m}^2$	[7]
Carbon paper tortuosity	$\tau_{MPS}$	1.199	[7]
Catalyst layer porosity	$\epsilon_{CL}$	0.497	[1]
Catalyst layer permeability	$\kappa_{CL}$	$8.82 \times 10^{-11} \text{ m}^2$	[1]
$O_3$ diffusion coefficient in $N_2$	$D_{O_3}$	$0.16 \text{ cm}^2 \text{ s}^{-1}$	[8, 9]
$O_3$ apparent reaction rate constant <sup>a</sup>	$k_{app}$	$250 \text{ s}^{-1}$	[1]

<sup>a</sup> Parameter used only in the original (Alpha) model.

Finally, for the sake of reference, the mesh used in [1] followed a custom-made procedure, based on the software’s recommendations, with ca.  $1.7 \times 10^6$  domain elements. The set of equations was solved using a two-step segregated solver, with each step using an implementation of the PARDISO[10] linear solver, to a relative tolerance of  $10^{-3}$ . A parametric solver was used to vary the inlet flow rate, with initial value  $Q = 200 \text{ cm}^3 \text{ min}^{-1}$  and a step of  $\delta Q = 50 \text{ cm}^3 \text{ min}^{-1}$  up to  $450 \text{ cm}^3 \text{ min}^{-1}$ , where each solution was used as the next step’s initial value.

## 2. Improved model

The improvements were largely implemented in the species transport formulation, with a closely related addition of surface cover kinetics, and two relatively minor changes. Additional parameters relevant only to the improved model are given in Table III.

TABLE III: Parameters relevant to the improved model.

Parameter	Symbol	Value	Reference
Average molar mass of dry air	$M_{\text{air}}$	$28.96546 \text{ g mol}^{-1}$	[11]
O <sub>3</sub> adsorption reaction rate constant	$k_1$	$100 \text{ s}^{-1}$	see text
O <sub>3</sub> (ads) decomposition reaction rate constant	$k_2$	$10 \text{ s}^{-1}$	see text
Average silica particle radius	$r_p$	$6.5 \text{ }\mu\text{m}$	see text
Quantity of dye deposited on the CL	$\Gamma_{\text{dye}}$	$3 \text{ }\mu\text{mol cm}^{-2}$	[2]

The main change in the model, which brings about most others as consequence, was the use of a concentrated-species approach to the fluid, which uses the following statement of species conservation, i.e. the advection-reaction equation:

$$\nabla \cdot \mathbf{J}_i + \rho (\mathbf{u} \cdot \nabla) \omega_i = R_i, \quad (7)$$

where  $\omega_i$  is the mass fraction of the  $i$ -th species, while the *mass* diffusive flux is given by the Maxwell-Stefan (MS) model:

$$\mathbf{J}_i = - \left( \rho \omega_i \sum_k D_{ik} \mathbf{d}_k \right) \quad (8)$$

$$\mathbf{d}_k = \nabla \chi_k + \frac{[(\chi_k - \omega_k) \nabla P_A]}{P_A}, \quad (9)$$

where  $D_{ik}$  are multi-component diffusivities,  $\mathbf{d}_k$  is a so-called diffusional driving force,  $\chi_k$  is the molar fraction and  $P_A$  is the absolute pressure. According to the User Guide for COMSOL's Batteries and Fuel Cells module, in the version used the  $D_{ik}$  are multi-component Fick diffusivities, which are obtained from the MS diffusion matrix by solving the following relation:

$$\frac{\chi_i \chi_k}{D_{ik}^{\text{MS}}} = -\omega_i \omega_k \frac{\sum_{j \neq i} (\text{adj} B_i)_{jk}}{\sum_{j \neq i} D_{ij} (\text{adj} B_i)_{jk}}, \quad (10)$$

where  $D_{ik}^{\text{MS}}$  are the binary MS diffusion coefficients,  $(B_i)_{kj} = D_{kj} - D_{ij}$ , for  $i \neq j$ , and  $\text{adj}$  stands for the adjoint operation  $\text{adj}(A_{ij}) = A_{ji}^*$ , where  $*$  is the complex conjugate. Both the MS and multi-component Fick diffusion matrices are symmetric. Furthermore, for two- and three-component mixtures, the software has analytical expressions for  $D_{ik}$  implemented, while for four components or more a numerical procedure is used. In addition to multi-component diffusion, the Knudsen regime was implemented for porous media transport:

$$D_{ij}^{\text{MS}} = \left[ \frac{1}{D_{ij}^{\text{Pm}}} + \frac{1}{D_{ij}^K} \right]^{-1}. \quad (11)$$

Here two effects are added in a parallel-resistances fashion: i) the porous media diffusion coefficient,  $D_{ij}^{\text{Pm}}$ , which follows Eq. 4; and ii) the Knudsen regime diffusivity, obtained through kinetic theory:

$$D_i^K = \frac{d_p}{3} \sqrt{\frac{8RT}{\pi M_i}}, \quad (12)$$

where  $d_p$  is the average pore diameter, commonly used instead of the mean free path in porous media,  $R$  is the gas constant,  $T$  is the temperature and  $M_i$  is the molar mass. In this case, the average pore diameter is obtained using the Millington & Quirk model for cemented particle beds[5] for simplicity. It will be noticed that Eq. 12 is written for a single species, and it is not clear how a binary Knudsen diffusion coefficient should be expressed. One option would be to calculate an average molar mass between a pair of species, weighed by their relative molar fractions. Another would be to sum the individual coefficients in a similar fashion as Eq. 11, weighed by their relative molar fractions. While this may be worthwhile to investigate, it is neglected at this point, as explained below.

At this point a few issues should be addressed. First, by switching to the MS model, the  $D_{\text{O}_3}$  used in Eq. 3 is no longer valid, being necessary appropriate MS binary diffusivities instead. Due to the difficulty of obtaining these coefficients, and given that the concentration

of ozone is small, whereas that of  $N_2$  and  $O_2$  are approximately constant, the value given in Table II is still used. Second, given the already pointed out constant relative concentrations of  $N_2$  and  $O_2$ , and to minimize computational costs, the components of the mixture were  $O_3$  and “air”, the latter with a molar mass of  $M_{\text{air}}$  (see Table III). In Section II of the Supplemental Material[12] (SM) a comparison is made between results using  $O_3/O_2/N_2$  or  $O_3/\text{air}$  mixtures. See also Section III C for a brief discussion on this issue.

Third and last, it is not clear at this moment how the different phenomena affecting diffusion couple together, such as shown in Eq. 11. For instance, whether it is appropriate to correct the free diffusion coefficient before calculating the multi-component Fick diffusivities, or, given the formulation and software limitations, how to correctly couple the individual Knudsen diffusivities to the Maxwell-Stefan diffusivities. The approach used here relies on the approximation of the constant  $N_2/O_2$  mixture as “air”, which results in a single entry to the MS diffusion matrix, then assuming ozone as being the sole contribution to the term ( $M_i = M_{O_3}$ ). It is also understood that the porous media affect species transport despite the contribution of the Knudsen regime, thus the application of the correction factor in Eq. 11. Section III of the SM provides a comparison with a few possibilities regarding this issue, in order to illustrate the expected effects in the system under study. Section III C also provides some discussion around this issue.

Back to the mathematical formulation, the reaction involving ozone degradation, and hence light emission, was modified to include the interaction with the dye molecule in an adsorption-desorption step, then leading to decomposition:



where the dye molecule is 7-diethylamino-4-methylcoumarin[2]. In this way, a new variable was defined,  $\theta_{O_3}$ , representing the surface coverage of ozone, with kinetics modeled by the differential equation:

$$\frac{d\theta_{O_3}}{dt} = k_1 c_{O_3} \chi_{O_3} (1 - \theta_{O_3}) - k_{-1} \theta_{O_3} - k_2 \theta_{O_3}, \quad (15)$$

where  $c_{O_3}$  is the ratio of the appropriate activity coefficients for bulk and adsorbed  $O_3$ ,  $k_1$  and  $k_{-1}$  are the forward and backward reaction rate constants for the adsorption-desorption reaction, respectively, and  $k_2$  is the reaction rate constant for the decomposition reaction.



Eq. 15 can be written as function of alternative variables concerning  $O_3$ , such as mass fraction or density, with the appropriate factors incorporated in the reaction rate constant. To couple with Eq. 7, one may write:

$$A_v \Gamma_s^* \frac{d\theta_{O_3}}{dt} = R_{O_3,ads}, \quad (16)$$

which corresponds to the total reaction rate for the adsorbed ozone over the CL domain, in  $\text{mol s}^{-1}$ , given that  $A_v$  is the total surface area by unit volume and  $\Gamma_s^*$  is the total surface concentration of active sites, i.e. dye molecules (see below). Thus, by excluding the last term of Eq. 15, one may write the sink term for bulk ozone as:

$$R_{O_3} = -M_{O_3} R_{O_3,ads} - M_{O_3} A_v \Gamma_s^* k_2 \theta_{O_3} \quad (17)$$

since the source/sink term in Eq. 7 is given in units of  $\text{kg m}^{-3} \text{s}^{-1}$ . For simplicity, the desorption term was neglected, thus leaving the sink term as:

$$R_{O_3} = -M_{O_3} A_v \Gamma_s^* k_1 \chi_{O_3} (1 - \theta_{O_3}), \quad (18)$$

where it was further assumed that  $c_{O_3} \approx 1$ . The total surface concentration of adsorption sites can be obtained with:

$$\Gamma_s^* = \frac{\Gamma_{\text{dye}}}{t_{\text{CL}} A_v}, \quad (19)$$

where  $\Gamma_{\text{dye}}$  is the reported[2] quantity of dye deposited over a given geometric area of CL with thickness  $t_{\text{CL}}$ . The  $A_v$  can, in principle, be determined experimentally, but for now it is calculated using a simple model:

$$A_v = \frac{3\epsilon_{\text{CL}}}{r_p}, \quad (20)$$

where  $r_p$  is the average particle radius, in this case the silica particles where the dye were anchored on (Nano Silica Gel, Sigma Aldrich).

Regarding the minor changes, the first concerns the inlet boundary condition in the momentum transport: a (standard) mass flow rate condition is now being used:

$$-\int_{\partial\Omega} \frac{\rho}{\rho_{\text{std}}} (\mathbf{u} \cdot \mathbf{n}) dS = Q, \quad (21)$$

with dry air at  $T_{\text{std}} = 273.15 \text{ K}$  and  $P_{\text{std}} = 1 \text{ atm}$  defining the standard density  $\rho_{\text{std}} = P_{\text{std}} M_{\text{air}} / RT_{\text{std}}$ . The fluid's density is still given by the ideal gas law, but now it is subjected

to the composition given by the species transport equations above; while the viscosity is given by a constitutive relation for air, given by the software:

$$\begin{aligned}\mu_{\text{air}}(T) = & -8.38278 \times 10^{-7} + 8.35717342 \times 10^{-8}T - 7.69429583 \times 10^{-11}T^2 \\ & + 4.6437266 \times 10^{-14}T^3 - 1.06585607 \times 10^{-17}T^4,\end{aligned}\tag{22}$$

where  $\mu_{\text{air}}$  has units of Pa s and  $T$  of K.

The last change implemented concerns the geometry of the computational domains, and is related to the mesh convergence study described in the next section. The full geometry was assembled as two distinct geometric entities: the Ch and the porous media. The Ch domain follows the description in [1], with the following modifications: i) the inlet and outlet sections were extended to fully cover the supporting plates existing in the experimental prototype (7 mm)[2], and ii) the upper boundary, partly in contact with the MPS, was segmented in two, corresponding to the section in contact with the MPS and the remaining part, closer to the inlet. The porous media domains are simply rectangular-shaped domains, with the addition of a copy of the Ch upper boundary at the lower boundary of the MPS, representing the part of the boundary in contact with the Ch domain. Figures 1c and 1d illustrates the points above.

The changes in the geometry were made in order to appropriately separate the meshes (and meshing procedure) of each geometric entity, thus allowing a greater control of the meshing procedure. As a consequence of these changes, explicit coupling between the geometric entities was needed to ensure the proper continuity of the model's variables, i.e. the flow field,  $\mathbf{u}$ , and ozone mass fraction,  $\omega_{\text{O}_3}$ . This was accomplished via an identity pair. Since the relevant boundaries were sectioned to properly match one another (at the Ch and MPS domains), no fallback features were necessary.

The solver configuration depends on the actual mesh used, however it followed a general configuration according to the number of mesh elements. A detailed description, as much as possible, can be found in Section IV.A of the SM. The general outline is the following: a segregated 3-steps solver was employed, with step i) solving for  $\theta_{\text{O}_3}$ , step ii) solving for  $\mathbf{u}$  and  $P$ , and step iii) solving for  $\omega_{\text{O}_3}$ . Step i) always employed a direct solver, based on MUMPS[13, 14], while step ii) always employed an iterative solver based on GMRES[15] with a multigrid scheme as preconditioner, where the number of levels and mesh coarsening scheme depend on the number of mesh elements. Step iii) either employed a direct solver,

also MUMPS-based, or a GMRES-based iterative solver using the domain decomposition method[16]. The direct solver was employed for the cases where  $\lambda \leq 4$ , otherwise the iterative solver was used, with the number of sub-domains depending on the number of mesh elements. All steps used a constant dampening factor in all cases, being 1.0, 1.0 and 0.7 for steps i), ii) and iii), respectively. In addition, a parametric solver was used to vary  $Q$  from 200 to 450 cm<sup>3</sup> min<sup>-1</sup> with a step of 50 cm<sup>3</sup> min<sup>-1</sup>, with the previous solution used as initial value for the next one.

## B. Mesh Convergence Study

### 1. Algorithm and refinement procedure

As mentioned above, the model’s geometry was an assembly of two geometric entities, the flow channel (Ch) and the porous media (Pm). This separation was used in order to achieve a larger degree of control with respect to the meshing procedure, allowing, for example, meshing the Ch and Pm domains separately in order to investigate the effects of each mesh individually. Following much experimentation, a protocol was established in order to assess mesh convergence in all domains, with respect to a single index,  $\lambda$ , which is somewhat connected to the more usual element spacing  $h$  in structured meshes. The meshing algorithm, briefly, had the following outline:

1. Meshing of the Ch domain with tetrahedral elements, with scaling factor  $\lambda$ .
2. Splicing the boundary-adjacent elements to add 3 hexahedral elements (“boundary layer elements”, BLEs).
3. Copying the mesh of the upper boundary of Ch to the projection onto the lower MPS boundary.
4. Meshing the remainder of the lower MPS boundary with triangular elements, with scaling factor 1.
5. Extruding the lower boundary elements throughout the Pm domains, with  $\lambda$  elements in each domain.

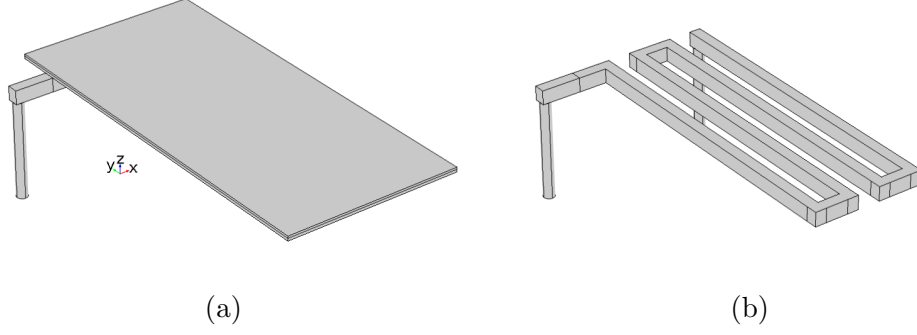


FIG. 2: Reduced geometry used in the proto-cell simulations with dense meshes: **(a)** full geometry, showing both Ch and Pm domains, and **(b)** Ch domain.

The element size parameters used in steps 1 and 4 were based on software recommendations, which in turn are believed to be based on the size of the full geometry. The so-called BLEs of step 2 are a software recommendation when dealing with relatively coarse meshes. A variant of this meshing algorithm without step 2 was also used. Details of the algorithm and of each mesh are given in Section IV.B of the SM, along with Fig. S8 illustrating the meshes built.

Given the current computational resources available, a reduced version of the geometry was employed to solve the model when using dense meshes. The Ch domain was shortened to 4 horizontal sections of the serpentine geometry, down from 10, as shown in Figure 2. The Pm domains were reduced accordingly, with the remaining geometric parameters kept constant. In this way, the scaling factor  $\lambda$  for the reduced geometry takes the values  $\lambda \in [2, 4, 8, 10, 12, 16]$ , while for the full geometry it reduces to  $\lambda \in [2, 4, 8, 12]$ .

## 2. Convergence analysis

Four variables were tracked in order to assess mesh convergence. These are of experimental interest, and, with the exception of the speed profiles, are readily available given the experimental setup[2]. These were selected to allow comparison between the reduced and full geometries, as well as between old and present model formulations (see Section II C). It is understood that some variables are functionals of the base variables solved in the model, and thus might not be as sensitive to the mesh. The chosen variables are the following:

- the ratio between reactant consumption,  $\Delta\chi_{\text{O}_3}$ , and the apparent reaction rate  $R'_{\text{O}_3}$ ;

- pressure drop,  $\Delta P$ , normalized by the inlet pressure,  $P_{\text{in}}$ ;
- the flow speed profile,  $U$ , along the  $x$  and  $z$  axes; and
- the ozone partial pressure,  $P_{\text{O}_3}$ , along the  $x$  axis.

Concerning the acquisition of the data from the model, Figure 3 shows, for the reduced geometry, the geometric entities used. The same are used for the full geometry, when appropriately scaled. A brief description of the adopted procedure follows.  $\Delta\chi_{\text{O}_3}$  and  $\Delta P$  are simply the differences in value between inlet and outlet averages, while  $P_{\text{in}}$  is the inlet average pressure.  $R'_{\text{O}_3}$  is given by integration over the upper CL boundary (Fig. 3a) of the term  $A_v\Gamma_s^*k_2\theta_{\text{O}_3}$ , which is the volume-averaged decomposition term for  $\theta_{\text{O}_3}$ . The  $U$  profiles were obtained at mid-length of the third horizontal section (Figs. 3b and 3c), where the  $x$  axis profile was obtained at mid-height, while the  $z$  axis profile was obtained at mid-width. The  $P_{\text{O}_3}$  was obtained at the upper CL boundary (Fig. 3d), along a line parallel to the  $x$  axis, passing over the turn sections of the flow channel.

In addition to the variables mentioned above, some spatially-resolved variables were also acquired, albeit mainly as illustrations of the effects of grid resolution. These are the ozone partial pressure surface  $\mathbf{P}_{\text{O}_3}$ , obtained at the upper CL boundary, and  $\mathbf{U}$  surfaces, obtained with a  $xy$  plane mid-height of the Ch domain and a  $yz$  plane cutting the middle of the second turn, before the section where the  $U$  profiles were taken. Finally, some variables were obtained to explore secondary issues, not related to mesh convergence. These were i) additional  $P_{\text{O}_3}$  profiles, parallel to the one shown in Fig. 3d, obtained at different  $y$  values:  $y_1 = (l_c - w_c)/2$  (shown in Fig. 3d),  $y_2 = y_1 - (w_c + w_l)$  and  $y_3 = 0$ . And ii) components of the ozone total molar flux vector, i.e. diffusive and convective, given by the 1st and 2nd terms of Eq. 7 respectively. These were acquired in the following situations: the  $z$ -component of a given molar flux vector, integrated over the boundary between Ch and MPS domains, or MPS and CL domains; and the magnitude of a given molar flux vector, averaged over the MPS or CL domains.

In order to quantitatively assess mesh convergence, the scalar variables, i.e.  $\Delta\chi_{\text{O}_3}/R'_{\text{O}_3}$  and  $\Delta P/P_{\text{in}}$ , were analyzed within the framework of the grid convergence index (GCI), as reviewed by Roache[17]. Thus, the generalized Richardson extrapolation was employed to provide an estimate on the error given by the discretization of the computational domains.

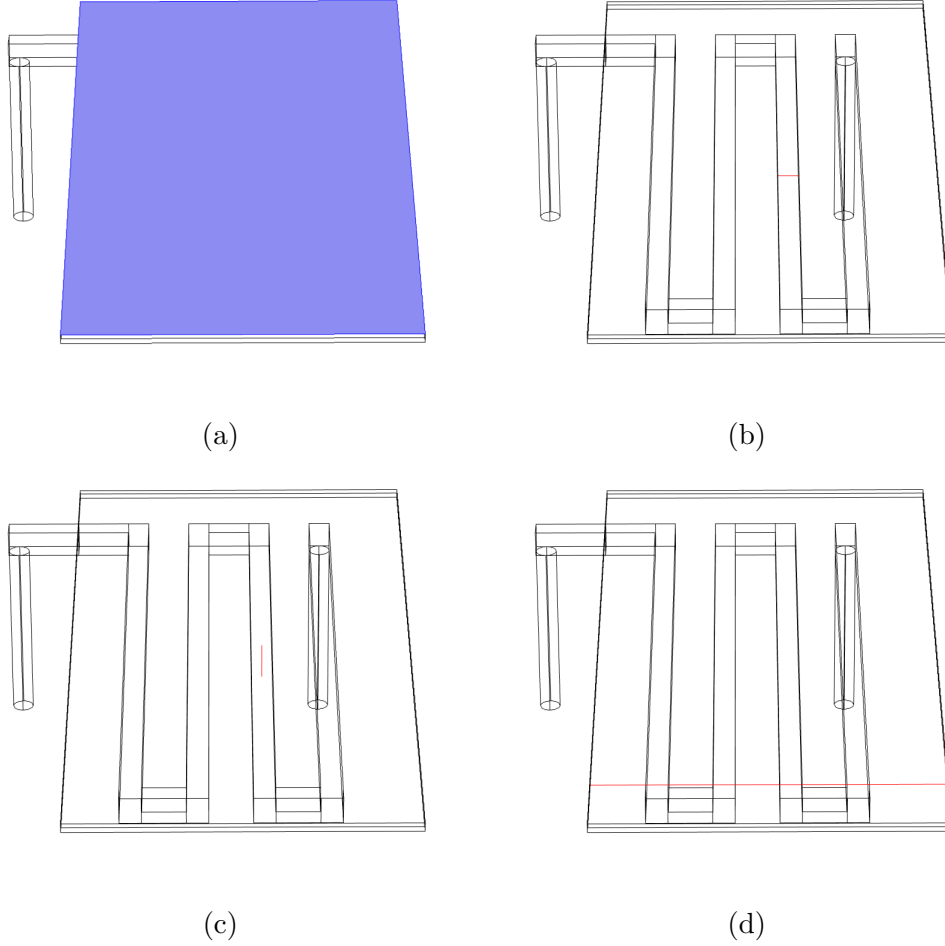


FIG. 3: Geometrical entities used to obtain the variables relevant for mesh convergence, shown for the reduced geometry: **(a)** **surface** used to obtain the apparent reaction rate, corresponding to the upper boundary of the CL domain; **(b,c)** **lines** used to track the flow speed  $x$  and  $z$  profiles, respectively; and **(d)** **line** used to track the ozone partial pressure profile atop the CL domain.

First, the effective refinement factors were calculated using[17]:

$$r_{\text{eff}} = \left( \frac{N_{\text{finer}}}{N_{\text{coarser}}} \right)^{1/D}, \quad (23)$$

where  $N$  is the number of elements in a given mesh and  $D = 3$  is the dimensionality. Eq. 23 was also used to calculate an effective, normalized element spacing,  $h$ , used to plot and visually analyze the mesh convergence of the selected variables. For such effect, a mesh is chosen such that  $r_{\text{eff}} = h = 1$ , thus coarser meshes are given by  $h > 1$ . For the reduced geometry,  $\lambda = 16$  was used, while for the full geometry  $\lambda = 12$  was used. The orders

of accuracy,  $p$ , were all calculated iteratively following the suggestion given in [17] (Eq. 15 of [17]), as the refinement ratios were non-integers and not constant. The generalized Richardson extrapolation was then used to estimate the exact value for a given variable  $f$ , by comparing the finest grid solution to a coarser one:

$$\bar{f}_R = f_1 + \frac{\epsilon_{21}}{1 - r_{12}^p}, \quad (24)$$

where we use the commonly employed convention of referencing the finer mesh with index 1, and progressively coarser meshes as 2, 3 and so on;  $\epsilon_{21} = f_2 - f_1$  is the error, while  $r_{12}$  is the (effective) refinement factor between meshes 1 and 2. The GCI is then given by:

$$\text{GCI} = F_s |\bar{f}_R - f_1|, \quad (25)$$

where  $F_s$  is a safety factor, taken as  $F_s = 1.25$  in this case, following [17]. As mentioned above, the GCI is then used as an estimate to the error of the model due to the discretization of the computational domains.

In addition to the generalized Richardson extrapolation, a mixed-order extrapolation, described by Roy[18], was also employed. This extrapolation scheme has the advantage of not requiring the calculation of the order of accuracy, while potentially allowing non-monotonic behavior and singularities in the grid-dependent response of each variable. In this case, the discretized solution is given by a power series in  $h$ [18]:

$$f_k = f_{\text{exact}} + g_1 h_k + g_2 h_k^2 + \mathcal{O}(h_k^3), \quad (26)$$

where  $k$  stands for a given mesh index following the convention pointed out above. In [18], a 1st- and 2nd-order scheme is presented, with  $\bar{f}_M \approx f_{\text{exact}}$  being obtained by solving a set of three linear equations up to powers in  $h_k^2$ . It is also mentioned[18] that it is possible to include higher-order terms by coupling additional equations, and thus meshes, in order to increase the order of the extrapolation. The error estimate is then calculated following a simple error calculation:

$$\epsilon_M = F_s |\bar{f}_M - f_1|, \quad (27)$$

where it can be seen that it is essentially the same as Eq. 25, when using the Richardson extrapolation to estimate the exact value[19].

### C. Comparison between Models

The models described in Section II A were compared to each other, with the previously published[1] model being referred to as *Alpha*, while the improved model was called *Beta*. Similarly to the mesh convergence analysis described above, experimentally relevant variables were analyzed, both qualitatively and quantitatively. Since the models use different species transport formulations, in particular concerning reaction terms, the ratio  $\Delta\chi_{\text{O}_3}/R'_{\text{O}_3}$  was primarily used for comparison. The individual variables,  $\Delta\chi_{\text{O}_3}$  and  $R_{\text{O}_3}$ , were also compared for the sake of completeness, however the differences in formulation and parameterization should be taken in account when analyzing the results. It should be noted that in the case of the Alpha model,  $R'_{\text{O}_3}$  was obtained directly from the integration of the sink term, Eq. 6, over the upper CL boundary (Fig. 3a). Variables solely related to the flow field, such as pressure drop and flow speed profile, were not expected to show significant changes since the formulations are basically the same, and thus are left to the SM.

In order to ascertain that differences between models are not due to mesh influence, both Alpha and Beta models were run using the mesh chosen after the convergence analysis (see Section III A, in particular Section III A 3). The chosen mesh was built using  $\lambda = 12$  without BLEs, following the scheme described in Section II B.

## III. RESULTS

As mentioned in Section I, first the results concerning the mesh convergence analysis shall be presented. The different mesh schemes and relevant variables analyzed are described in Section II B, and additional details can be found in the SM. Following some discussion considering mesh choice and error estimation, the original and improved models Alpha and Beta respectively, will be compared and discussed following Section II C.

### A. Mesh Convergence Study

#### 1. Reduced Geometry

We start with the analysis of the reduced model, in order to cover the full range of  $\lambda$  studied. Following Section II B 2, first the scalar variables will be analyzed, followed by the



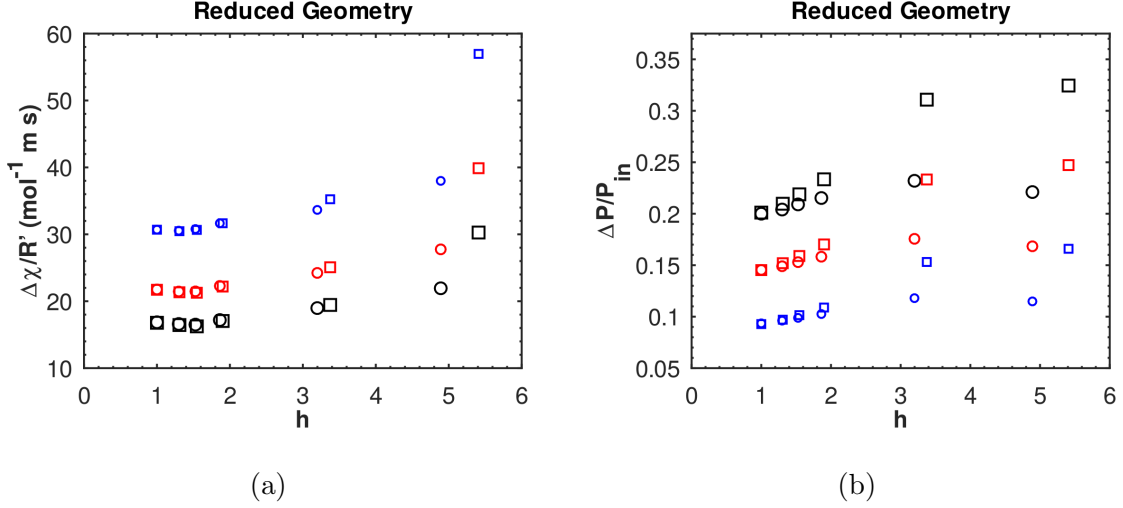


FIG. 4: Scalar variables as functions of the normalized effective element spacing, for the reduced geometry: **(a)**  $\Delta\chi_{\text{O}_3}/R'_{\text{O}_3}$  and **(b)**  $\Delta P/P_{\text{in}}$ . The following values of inlet flow rate  $Q$  are shown, with marker size increasing with  $Q$ : 250, 350 and 450  $\text{cm}^3 \text{min}^{-1}$ . Both mesh variants are shown: with BLEs ( $\circ$ ) and without ( $\square$ ).

speed and partial pressure profiles and finally the partial pressure surfaces. Thus, Figures 4a and 4b present the ratios  $\Delta\chi_{\text{O}_3}/R'_{\text{O}_3}$  and  $\Delta P/P_{\text{in}}$ , respectively, as a function of  $h$ . In each case both BLEs and no-BLEs study variants are shown (See Section II B 1). Individual variables are left to Section V of the SM (Fig. S9).

Readily apparent features of Fig. 4 are the large differences between the BLE and no-BLE variants at coarser meshes, i.e. high  $h$ , and the convergence of values at finer meshes, particularly for the  $\Delta\chi_{\text{O}_3}/R'_{\text{O}_3}$  ratio. In addition, it is seen that, for the  $\Delta P/P_{\text{in}}$  ratio, the existence of BLEs leads to a non-monotonic behavior in high  $h$ . Indeed, this is also seen for  $\Delta\chi_{\text{O}_3}$  (Fig. S9a) and  $\Delta P$  (Fig. S9c), while, notably,  $R'_{\text{O}_3}$  (Fig. Sb) shows such behavior for both mesh variants. The differences caused by the existence of BLEs, or likewise the absence of BLEs, are linked to a much better description of the velocity field  $\mathbf{u}$  in coarser meshes, as will be clear when discussing the speed profiles. Likewise, the non-monotonic behavior seen with  $R'_{\text{O}_3}$  is linked to the poor description of  $\mathbf{u}$  along the thickness of the Pm domains, and, consequently, to that of the ozone mass fraction  $\omega_{\text{O}_3}$ .

Additional features of Fig. 4 are the non-monotonic behavior of  $\Delta\chi_{\text{O}_3}/R'_{\text{O}_3}$  at low  $h$ , and a relatively slow convergence of  $\Delta P/P_{\text{in}}$ . It is not clear why  $\Delta\chi_{\text{O}_3}/R'_{\text{O}_3}$ , and likewise  $\Delta\chi_{\text{O}_3}$ , shows such behavior, or why is it dependent on  $Q$ . Suspicion once again resides

with  $\mathbf{u}$ , as does with the reason behind the slow convergence of  $\Delta P/P_{\text{in}}$  (and also of  $\Delta P$ ), and will be further explored below. Nevertheless, Roache[17] does point out that, far from the asymptotic regime, a variable can show non-monotonic behavior as function of element spacing. Indeed, considering the apparent lack of studies exploring mesh convergence in models of fuel cells and similar devices, an important result of this work is exactly the demonstration that experimentally relevant variables, even functionals of base variables, show non-monotonic behavior in a relatively wide range of  $h$  for 3D unstructured meshes. Thus, rather unfortunately, demonstrating mesh convergence for experimentally relevant variables in fuel cells may be a harder case than usually assumed.

We now proceed to analyze the profiles, starting with the speed profiles,  $U$ . Figure 5 shows the  $U$  profiles parallel to  $x$  and  $z$  axes, at  $Q = 350 \text{ cm}^3 \text{ min}^{-1}$ . Once again it is seen a marked difference between meshes with and without BLEs at high  $h$  (low  $\lambda$ ). As pointed out above, such marked differences at high  $h$  are thought to be responsible for the distinct behaviors seen for each mesh variant in Figs. 4 (likewise in Figs. S9). The absence of BLEs leads to a large underestimation of  $U$  in the Ch domain, which is known to contribute significantly to reactant transport to the Pm domains[1], thus affecting total reaction rate and reactant consumption. It is clear, then, from Figs. 5a and 5b that the presence of BLEs provides a much needed resolution close to the Ch walls, however that necessity fades as the mesh improves. Indeed, at  $\lambda = 12$  the mesh variants display close similarity, with an average difference of  $\approx 3.5\%$  for both  $x$  and  $z$  profiles.

Concerning the dependence of  $U$  with  $h$ , it can be seen that, as  $h \rightarrow 0$ , the flow in the Ch domain assumes a Poiseuille-like shape, i.e. parabolic as function of wall distance. This is of course expected at the center of the channel, for a well-developed flow field, and suggests that meshes with  $\lambda \geq 12$  provide a good description of the flow field. A similar trend is seen in Fig. 5c for the CL, however with an initial overestimation of  $U$  and a sharp gradient along  $z$ . This poor description of  $U$ , when comparing  $\lambda = 2$  to 16, might be related to the non-monotonic behavior observed for  $R'_{\text{O}_3}$  (Fig. S9b) at high  $h$ : while  $U$  is overestimated at the peak, the sharp gradient leading to  $U = 0$  at the CL upper boundary might contribute to lower rates of  $\text{O}_3$  transport to the surface, thus reducing the observed value of  $R'_{\text{O}_3}$ . For the MPS, on the other hand,  $U$  takes a more complex shape that is quite inappropriately modeled for  $\lambda \leq 4$ . Such profile is thought to result from the interaction with the Ch and CL domains, where both have larger permeabilities than the MPS (with  $\kappa_{\text{Ch}} \rightarrow \infty$ ). While the

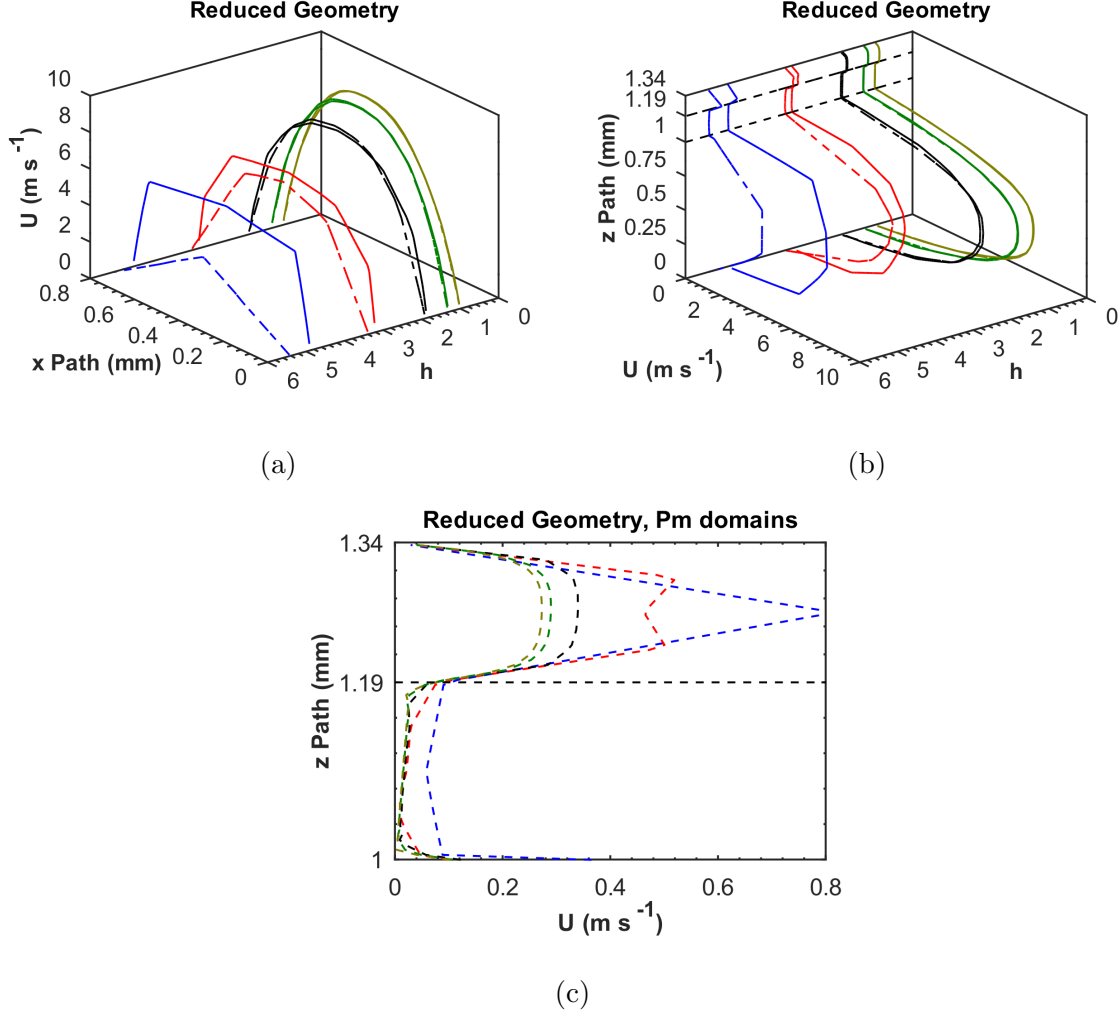


FIG. 5: Flow speed profiles as functions of the normalized effective element spacing, for  $Q = 350 \text{ cm}^3 \text{ min}^{-1}$ : **(a)** profile along the  $x$  axis, **(b)** along the  $z$  axis, with **(c)** zoom in on the Pm domains. Both BLE (full lines) and no-BLEs (dashed lines) mesh variants are shown. The following values of  $\lambda$  are shown: 2, 4, 8, 12, and 16. In **(b)** the dashed black lines in the  $yz$  plane correspond to the boundaries between Ch and MPS, and MPS and CL domains, while in **(c)** the MPS-CL boundary is depicted.

case of coupled free and porous media flow is widely studied in general, when approaching the problem analytically it is common to assume a semi-infinite porous medium domain (see for instance [4, 20]), which leads to a transition zone at the boundary and a plug flow in the porous medium that is typical of Darcy's law. Interactions between porous media, or walls, are less explored and possibly quite idiosyncratic, leading to unconventional effects (see for instance [21]). Thus, it is difficult to judge if the  $U$  profile in the Pm is well-described,

as some changes are still noticeable between  $\lambda = 12$  and 16 (see Section III B and Section VIII.B of SM).

Another point worth noticing concerns the symmetry of the  $U$  profiles with wall distance. While it is not clear in Fig. 5, and the effect is somewhat subtle, the improved description of  $\mathbf{u}$  as  $\lambda$  increases allows modeling finer structures that might provide additional insight on the interpretation of experimental results. Figure 6 shows superimposed  $U$  profiles of the no-BLEs mesh variant, for  $\lambda \geq 8$  and selected values of  $Q$ . For the sake of visibility the BLEs variant is not shown, however it does show the same trends discussed below, as suggested by the close agreement between mesh variants shown in Fig. 5. For the  $x$  profiles (Fig. 6a) it can be seen that, for  $\lambda = 8$ ,  $U$  is virtually symmetric around the center of the channel, even as  $Q$  increases. As  $\lambda$  increases, however, it becomes increasingly apparent that  $U$  is not symmetric, in particular for high  $Q$ . It is noteworthy that for  $\lambda = 16$  the  $U$  profile is asymmetric throughout the  $Q$  range simulated. This is likely to be an effect of secondary flows at the turns of the channel, which are better resolved the finer the mesh. This will be further explored below, but it already points out that the turns of a serpentine flow channel have far-reaching effects on the flow field, besides the fact that it greatly contributes to the convective transport in the porous media[1]. Regarding the  $z$  profiles (Fig. 6b), the asymmetry in  $U$  is much more subtle: there are virtually no deviations for  $\lambda = 8$  and 12 throughout the  $Q$  range, while  $\lambda = 16$  shows some asymmetry at  $Q \geq 350 \text{ cm}^3 \text{ min}^{-1}$ , becoming apparent at  $450 \text{ cm}^3 \text{ min}^{-1}$ . This effect appears to be caused by the porous interface, between Ch and MPS domains, as no such asymmetry is seen when a no-slip boundary condition is set instead (not shown). It is not clear, however, if it is also related to the turns of the flow channel.

We sidetrack now for a moment to consider the spatially-resolved  $U$  surfaces, in order to get a glimpse on the effects of the mesh on  $\mathbf{u}$  as mentioned above. Figure 7 shows  $U$  surfaces, for  $\lambda \in [8, 12, 16]$  and  $Q = 350 \text{ cm}^3 \text{ min}^{-1}$ , at the second turn of the serpentine Ch domain. Figures 7a to 7c show a mid-height  $xy$  plane, where it is readily noted the existence of known secondary flows, due to the corners and from boundary layer separation (BLS). While real turns are not 90 deg sharp, it has been shown, albeit indirectly, that the simulated flow field correlates quite well with experiments[1, 2]. As  $\lambda$  increases, a larger effect of the BLS is noticed, and recirculation at the corners become better resolved. Better resolution is of course the whole point, however it is noteworthy how the improved description of the

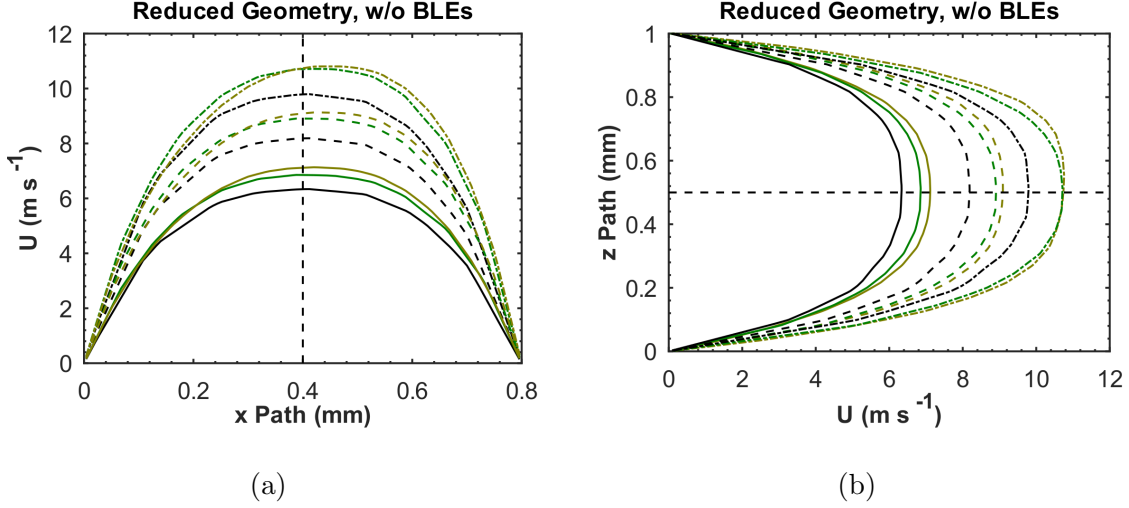


FIG. 6: Flow speed profiles for selected values of  $\lambda$  and  $Q$ , using the no-BLEs mesh variant: (a) profile along the  $x$  axis and (b) along the  $z$  axis. The following values of  $\lambda$  are shown: 8, 12, and 16. The following values of  $Q$  are shown: 250 (full), 350 (dash), and  $450 \text{ cm}^3 \text{ min}^{-1}$  (dash-dot). The dashed black lines parallel to the  $U$  axes are visual guides stressing the middle of the path along the Ch domain.

BLS significantly changes the flow field after the turn: at  $\lambda = 8$ , the flow field is almost completely re-developed at the end of the Ch section shown, while at  $\lambda = 16$ , there is a significant shift of the flow field to the right. This builds upon the discussion around Fig. 6a, establishing that BLS is a major source of the  $U$  profile asymmetry observed, and that fine grid resolution is needed to properly describe such effects. In addition to effects at the Ch domain, BLS is thus expected to impact on reactant distribution at the Pm domains. As shown in [1], secondary flows at the turns of serpentine Ch are major drivers of reactant distribution, therefore one would expect that the effect caused by BLS just uncovered might have implications as well. One such implication is a discrepancy between experimental and simulated  $\text{P}_{\text{O}_3}$  surfaces, noted in [1], concerning a broader plume of  $\text{O}_3$  along each horizontal section of the Ch in the experimental device. We shall come back to this point below, when analyzing  $\text{O}_3$  partial pressure.

It is also worth looking at the cross-section of the turn. It was shown in [1] that the turns of the serpentine Ch creates vortices, which are thought to contribute to reactant transport to the Pm domains. Figures 7d to 7f show  $U$  at a  $yz$  plane at the middle of the turn, also for  $\lambda \in [8, 12, 16]$  and  $Q = 350 \text{ cm}^3 \text{ min}^{-1}$ . Far from being a numerical artifact, it is indeed

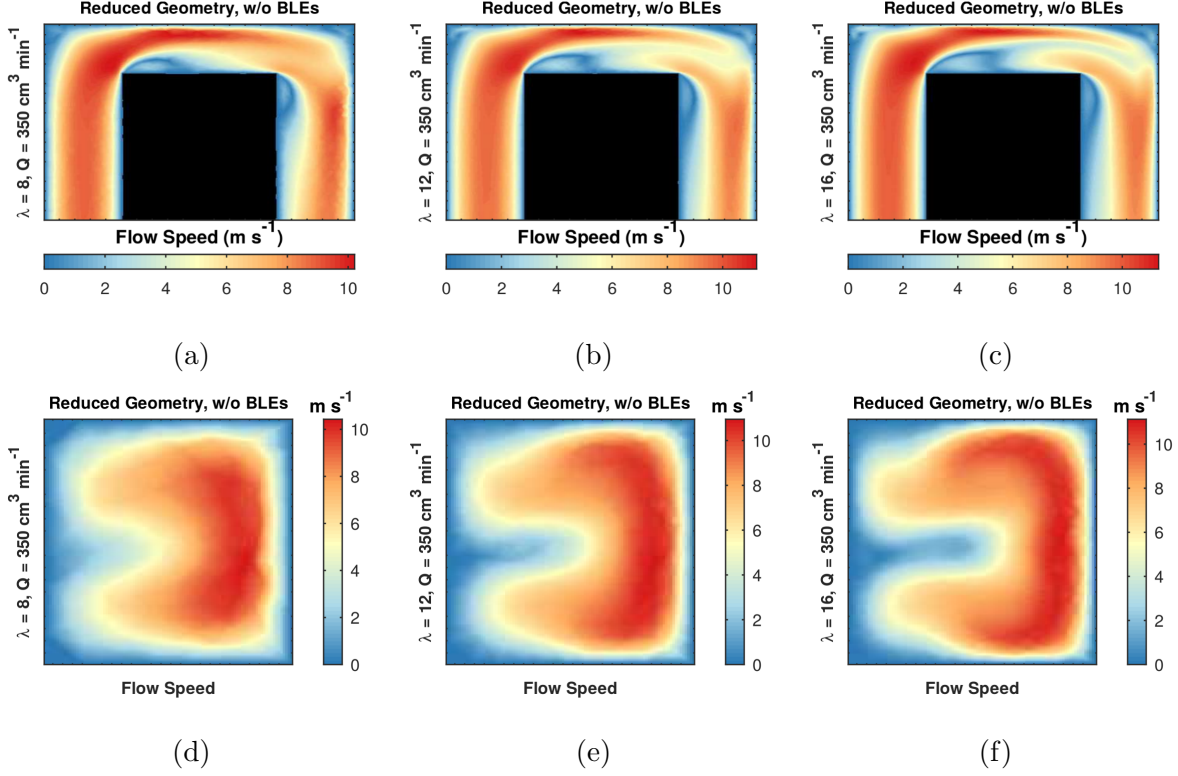


FIG. 7: Flow speed surfaces for selected values of  $\lambda$  and  $Q = 350 \text{ cm}^3 \text{ min}^{-1}$ , using the no-BLEs mesh variant: **(a-c)**  $xy$  plane mid-height of the 2nd turn of the Ch domain and **(d-f)**  $yz$  plane cutting through the middle of the turn. The values of  $\lambda$  sampled are indicated, and include  $\lambda = 8, 12$ , and  $16$ .

seen that these vortices are robust, and that increased grid resolution shows better defined structures, with higher  $U$  and possibly greater contribution to reactant transport.

In all, Figs. 6 and 7 provide further evidence that the flow field in fuel cell flow channels, in particular serpentine ones, are rather complex and require good grid resolution to properly capture its features. It also sheds some light on the convergence behavior of the scalar variables analyzed above (Fig. 4): i) there is a significant change in  $\mathbf{u}$  at  $\lambda > 8$ , which might underlie the non-monotonic behavior of the ratio  $\Delta\chi_{\text{O}_3}/R'_{\text{O}_3}$  at low  $h$  (or the individual variables), and ii) the grid resolution necessary to resolve such relatively small-scale structures might underlie the slow convergence rate of  $\Delta P/P_{\text{in}}$ . Thus, it is of utmost importance that grid convergence studies be performed before validating and actually employing fuel cell models for predictions.

Resuming our analysis, we move to the ozone partial pressure profiles,  $P_{\text{O}_3}$ . Figure 8 shows

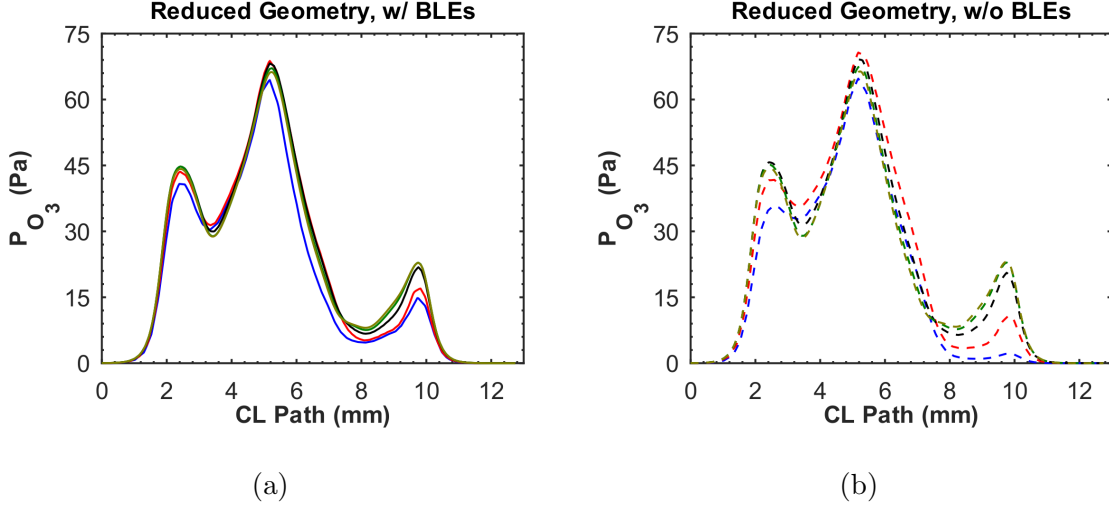


FIG. 8: Ozone partial pressure profiles, at  $Q = 350 \text{ cm}^3 \text{ min}^{-1}$ , for both mesh variants: **(a)** with BLEs (full line) and **(b)** without BLEs (dashed line). The following values of  $\lambda$  are shown: 2, 4, 8, 12, and 16.

the profiles obtained at the upper CL boundary, along the  $x$  axis, for  $Q = 350 \text{ cm}^3 \text{ min}^{-1}$ . Analyzing each mesh variant individually at first, it is observed that the BLEs variant (Fig. 8a) shows relatively little qualitative change, and progressively small changes as  $\lambda$  increases. On the other hand, the no-BLEs variant (Fig. 8b) show a marked increase in  $P_{\text{O}_3}$  at the end of the flow path, as  $\lambda$  increases. Nevertheless, when comparing both mesh variants, it can be noticed that their profiles are very similar at  $\lambda = 16$ , although their dependency on  $h$  is somewhat different. This is further illustrated on Fig. S10, where fewer values of  $\lambda$  are shown, and very small differences are seen between the variants at  $\lambda = 16$ . It is thus seen that the  $P_{\text{O}_3}$  profiles benefit from BLEs at high  $h$ , particularly at the end of the flow path.

Finally, in order to provide a broader, albeit qualitative view on the effects of the mesh on  $P_{\text{O}_3}$ , we will briefly analyze the ozone partial pressure surfaces,  $\mathbf{P}_{\text{O}_3}$ . Figure 9 presents such surfaces for selected values of  $\lambda$ , with  $Q = 350 \text{ cm}^3 \text{ min}^{-1}$ . The no-BLEs mesh variant is shown in order to highlight the changes as  $\lambda$  increases, however, in general, the changes follow those seen in Fig. 8. There are several trends that can be observed as  $\lambda$  increases: i) the increased  $P_{\text{O}_3}$  values at the end of the flow path, after the last turn; ii) an improved description of the local  $P_{\text{O}_3}$  maxima after each Ch turn; iii) a narrowing of the ozone plume along each horizontal section; and iv) a decrease of maximum  $P_{\text{O}_3}$  values. Trends i) and ii) are directly related to the improved description of  $\mathbf{u}$ , as seen in Figs. 5 and 7, which

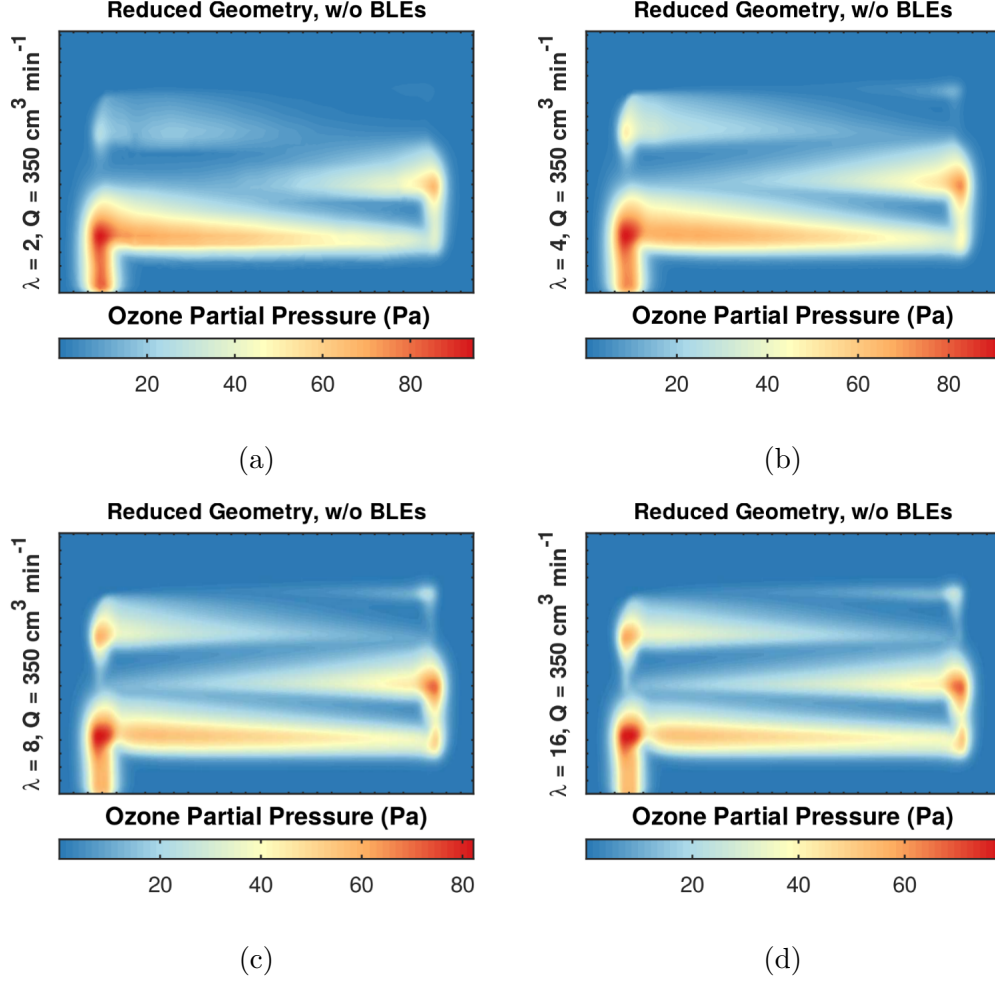


FIG. 9: Ozone partial pressure surfaces for selected values of  $\lambda$  and  $Q = 350 \text{ cm}^3 \text{ min}^{-1}$ , using the no-BLEs mesh variant: (a)  $\lambda = 2$ , (b)  $\lambda = 4$ , (c)  $\lambda = 8$ , and (d)  $\lambda = 16$ .

impacts not only  $P_{\text{O}_3}$  through better resolution, but also by reducing  $\Delta\chi_{\text{O}_3}$  (Figs. 4 and S9) and consequently allowing increased concentrations of ozone to reach the end section of the Ch domain. Skipping to trend iv), reduced  $P_{\text{O}_3}$  values might also be connected to  $\mathbf{u}$ , although it is thought that the increased resolution at the Pm domains might play a larger role in this case. In addition, smaller  $P_{\text{O}_3}$  values might also be related to the reduced  $\Delta\chi_{\text{O}_3}$  values at high  $\lambda$ , suggesting that increased influence of  $\mathbf{u}$ , possibly in the form of convective transport, impacts reactant distribution, thus reducing local  $P_{\text{O}_3}$  maxima.

Trend iii) is also thought to be connected to the improved description of  $\mathbf{u}$ , as well as improved resolution across the Pm domains' thickness. However it provides a counter-evidence to the point raised when analyzing Figs. 6 and 7. It was suggested that the



effect the BLS has on  $\mathbf{u}$  after each turn, that of deforming its  $x$  profile towards the wall, could underlie the broader reactant plume observed in the experimental  $P_{\text{O}_3}$  surfaces (see [2] for the original data and [1] for a comparison between experimental and numerical data). While  $\mathbf{u}$  at the Ch domain has a large influence on the Pm domains, and refining the grid indeed corroborates this point, it appears that this discrepancy between experimental and numerical data is not yet settled.

Trends iii) and iv) warrant some additional inspection, as it might be useful when considering numerical results with lower grid resolution. Following the inverted analysis of trends iii) and iv), we start by further analyzing trend iv), by looking into the reactant transport. Figure 10 presents the diffusive and convective contributions to  $\text{O}_3$  transport for selected values of  $\lambda$ , for the cases described in Section II B 2. From Figs. 10a and 10b it is seen that convective transport between domains increases with  $Q$ , as expected, while diffusive transport shows a maximum around  $Q = 300 \text{ cm}^3 \text{ min}^{-1}$ , between the Ch and MPS domains, and a slight increase with  $Q$  between MPS and CL domains. Concerning molar flux inside each Pm domain, Figs. 10c and 10d show that convective transport is the dominant process, observed the difference in permeability between domains and thus  $\mathbf{u}$  (see Fig. 5), showing large increase with  $Q$ , while the diffusive transport shows relatively little increase with  $Q$ . Overall, this picture corroborates the conclusions drawn from the previous study[1], where the convective transport is found to be a large contributor to reactant transport in all domains of the device. Concerning this work, Fig. 10 adds to the picture, showing that, in general, increased grid resolution ( $h \rightarrow 0$ ) leads to a decrease in convective transport, while the diffusive contribution slightly increases. This has the overall effect of reducing total  $\text{O}_3$  transport to the CL, and thus reducing  $P_{\text{O}_3}$  at the CL, as well as  $\Delta\chi_{\text{O}_3}$  and  $R'_{\text{O}_3}$  (see Fig. S11 for the explicit dependency on  $h$ ).

Returning once again to trend iii), additional insight may be obtained by considering  $P_{\text{O}_3}$  profiles normalized by  $R'_{\text{O}_3}$ . Figure 11 shows the  $P_{\text{O}_3}/R'_{\text{O}_3}$  profiles at three parallel lines along the  $x$  axis, described in Section II B 2 by  $y_1$ ,  $y_2$ , and  $y_3$ . Shown are selected values of  $\lambda$  and  $Q$  for the no-BLEs mesh variant, in order to illustrate the changes as either  $\lambda$  or  $Q$  increases. In all profiles it is seen that, contrary to Fig. 8, the local maxima corresponding to the Ch domain increases: while the absolute value of  $P_{\text{O}_3}$  may decrease as  $\lambda$  increases, the value relative to  $R'_{\text{O}_3}$  increases. This corroborates the scenario that, while the magnitude of the convective transport of reactant may decrease with  $\lambda$ , the improved description of  $\mathbf{u}$

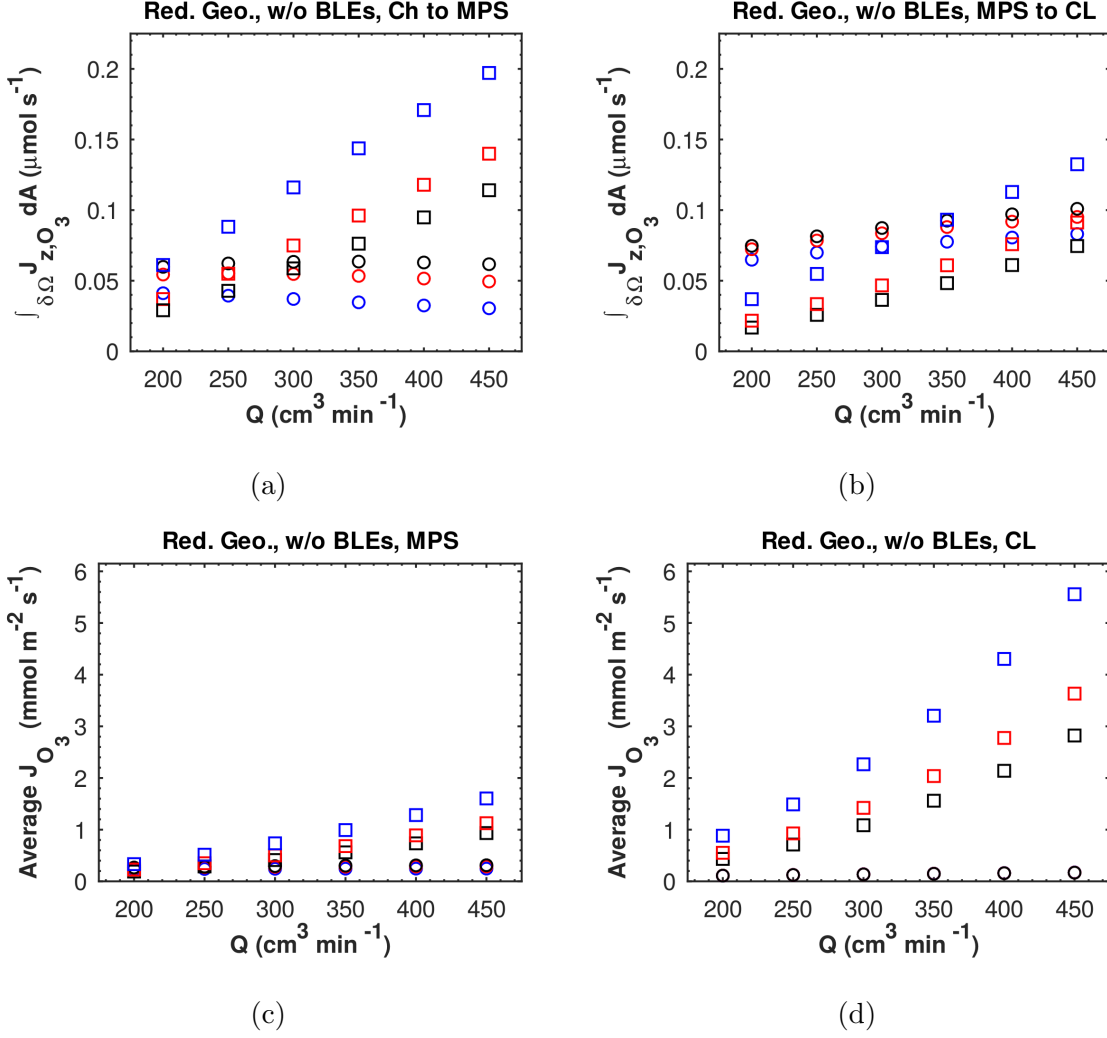


FIG. 10: Contributions to ozone molar flux as function of the flow rate, using the no-BLEs mesh variant, for selected values of  $\lambda$ : 4, 8, and 16. **(a)** integrated  $z$  component of the molar flux over the boundary between Ch and MPS domains, and **(b)** between MPS and CL domains; **(c)** average magnitude of the molar flux over the MPS and **(d)** domains. Both diffusive ( $\circ$ ) and convective ( $\square$ ) contributions to the total molar flux are shown.

given by the finer grids better capture the reactant distribution in the device. This is seen to be particularly important at the end of the flow path, where  $\lambda = 4$  greatly underestimates the local reactant distribution. Regarding trend iii) and the hypothesis discussed before, Fig. 11 settles the issue, showing that in fact the spread of the reactant plume, between Ch sections, decreases with  $\lambda$ . Increasing  $Q$  also increases the plume spread, as already seen in Fig. 9, as well as slightly shifting the local maxima towards higher  $x$  values, corroborating

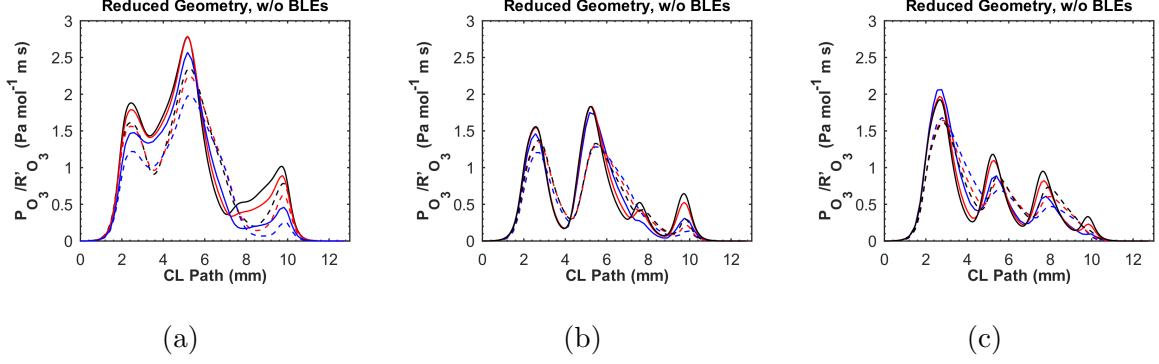


FIG. 11: Ozone partial pressure profiles, using the no-BLEs variant, for selected values of  $\lambda$ : 4, 8, and 16; and  $Q$ : 250 (full line) and 450  $\text{cm}^3 \text{min}^{-1}$  (dashed line). The profiles were obtained at the upper boundary of the  $CL$ , parallel to the  $x$  axis, according to Section II B 2: (a)  $y_1$ , shown in Fig. 3d; (b)  $y_2$ ; and (c)  $y_3$ .

the effects of the shifted  $U$  maximum seen in Fig. 6. Thus, while the improved description of  $\mathbf{u}$  in the Ch domain has effects throughout the Pm domains, it does not seem to be responsible for the reactant plume spread seen in the experimental data.

## 2. Full Geometry

We complete this first analysis with a brief comparison between the behavior of the reduced geometry, analyzed above, and that of the full geometry. Focus will be given to the largest values of  $\lambda$  used with the full geometry, 8 and 12, as well as the largest value used for the reduced geometry,  $\lambda = 16$ . In addition, only the no-BLEs mesh variant will be used, as the analysis above already shows that both mesh variants provide very similar results for  $\lambda \geq 12$ . The entire range of  $\lambda$  for the full geometry, as well as the BLEs mesh variant can be found in Section V.B of the SM (Figs. S12 to S19).

Once again we follow the order previously established, starting with the scalars described on Section II B 2. Figure 12 presents the  $\Delta\chi_{\text{O}_3}/R'_{\text{O}_3}$  and  $\Delta P/P_{\text{in}}$  ratios for both reduced and full geometries, as functions of a normalized effective element spacing  $h'$ , calculated with reference to the meshes with  $\lambda = 12$ . It can be seen that, for both scalars, the convergence behavior is very similar between reduced and full geometries. It should be pointed out, however, that the  $\Delta\chi_{\text{O}_3}/R'_{\text{O}_3}$  ratio displays a monotonic behavior for the full geometry. An additional mesh with  $\lambda = 10$  might help to draw this behavior out, although it is unnecessary

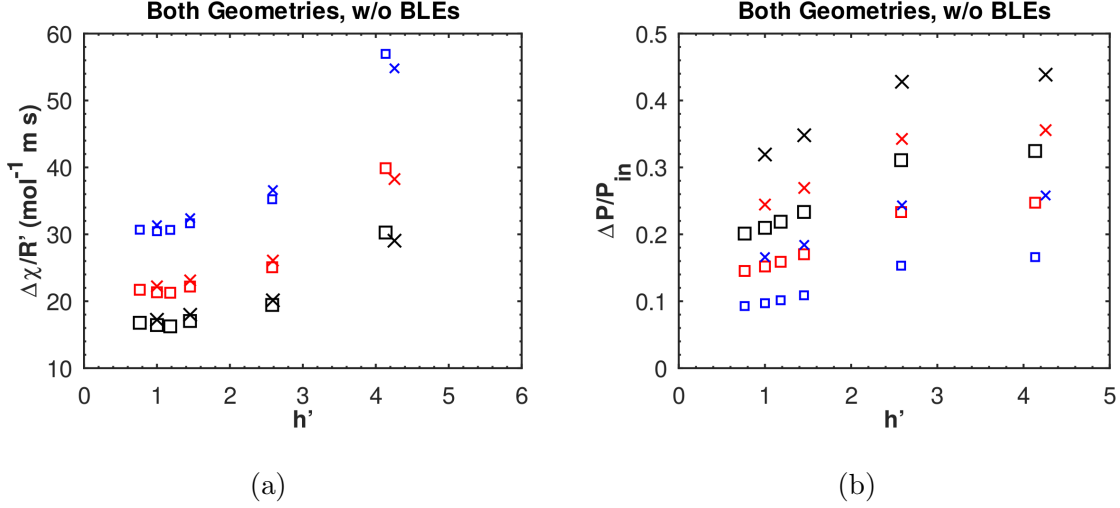


FIG. 12: Scalar variables as functions of the normalized effective element spacing, obtained for both reduced ( $\square$ ) and full ( $\times$ ) geometries: **(a)**  $\Delta\chi_{\text{O}_3}/R'_{\text{O}_3}$  and  $\Delta P/P_{\text{in}}$ . The following values of inlet flow rate  $Q$  are shown, with markers increasing in size with  $Q$ : 250, 350 and 450  $\text{cm}^3 \text{ min}^{-1}$ .

given that  $R'_{\text{O}_3}$  display non-monotonic behavior with  $h'$  (Fig. S12b). Care must be taken, therefore, in order to realize a fuller picture before drawing conclusions on grid convergence. Small differences in value, mainly seen in Fig. 12b, are likely due to the fact that the corners in the Ch domain contribute non-linearly to the overall results of the device, particularly for  $\Delta P$ . This is another evidence to the well-known fact that the scaling of fuel cells is not linear, in particular for serpentine-type flow channels.

Moving on to the  $U$  profiles, Figure 13 shows the  $x$  and  $z$  profiles for both geometries, superimposing values of  $\lambda$  and with  $Q = 350 \text{ cm}^3 \text{ min}^{-1}$ . It can be observed that both geometries have very similar  $U$  profiles, both in  $x$  and  $z$ , with the largest differences at the CL domain, while the MPS domain shows the smallest. This result is expected, given that the characteristic dimensions of the flow and  $Q$  are the same for both geometries. It is important nevertheless to be assured of this, given the already pointed out non-linear scaling of fuel cells, but also due to possible numerical artifacts.

Finally, the  $P_{\text{O}_3}$  profiles are compared in Figure 14, while the  $\mathbf{P}_{\text{O}_3}$  surfaces for the full geometry are shown in Figure 15, comparing them with the reduced geometry for  $\lambda = 12$  (see also Fig. 9). Regarding the  $P_{\text{O}_3}$  profiles, Fig. 14a shows close similarities between reduced and full geometries at the beginning of the flow path, with a marked distinction at

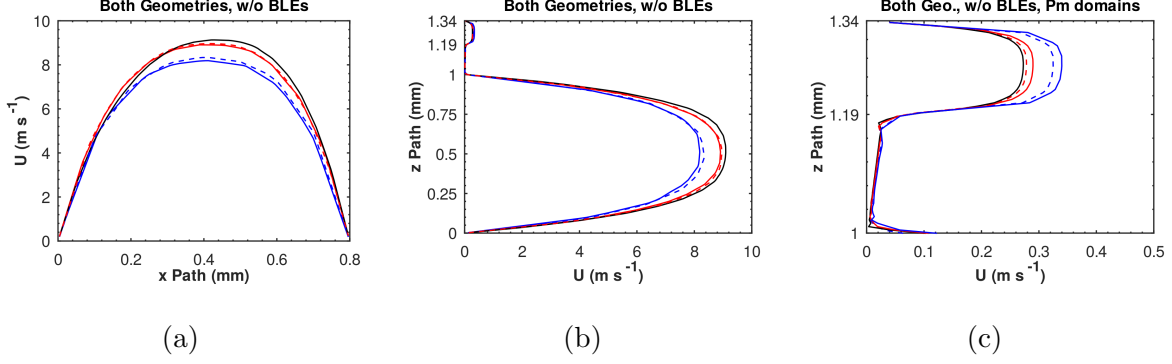


FIG. 13: Flow speed profiles for the reduced (full lines) and full (dashed lines) geometries, using the no-BLEs mesh variant, for  $Q = 350 \text{ cm}^3 \text{ min}^{-1}$ : (a) profile along the  $x$  axis, (b) along the  $z$  axis, with (c) zoom in on the Pm domains. The following values of  $\lambda$  are shown: 8, 12, and 16.

the last local peak. The similarities are once again to be expected, given the geometrical and operational parameters of each model. The significant difference at the last peak of Fig. 14a, while at first may stand out, is readily understood when noticing that in Fig. 14b the same happens for the full geometry: the last channel of the Ch domain has no gradients driving the reactant forward in the CL domain, thus acting only as the final sink. Fig. 14 thus shows once again that both reduced and full geometries have similar grid convergence behavior, while at the same time further illustrating the non-linear scaling of fuel cell devices.

Regarding the  $\mathbf{P}_{\text{O}_3}$  surfaces, shown in Fig. 15, the same behavior observed for the reduced geometry is seen when comparing  $\lambda = 8$  and 12 for the full geometry, however in smaller magnitude, given the smaller grid refinement between them. The clearer aspect to be seen is the decrease in maximum  $P_{\text{O}_3}$ , which follows the behavior seen in Fig. 9. When comparing both geometries, with the reduced one shown scaled in Fig. 15c for better comparison, it can be seen that the  $\mathbf{P}_{\text{O}_3}$  surfaces are very similar. The major difference is at the spread of the plume after the third peak in the reduced geometry, however that is clearly due to the interaction with the last section of the Ch, as pointed out above when analyzing Fig. 14. Indeed, the same behavior, albeit with much smaller  $P_{\text{O}_3}$  values, is seen at the ninth peak.

The data show that the reduced geometry is a good proxy to study mesh convergence in the fuel cell prototype's model, given that we are currently unable to simulate meshes with  $\lambda > 12$  for the full geometry. Having shown this correlation between geometries, it opens

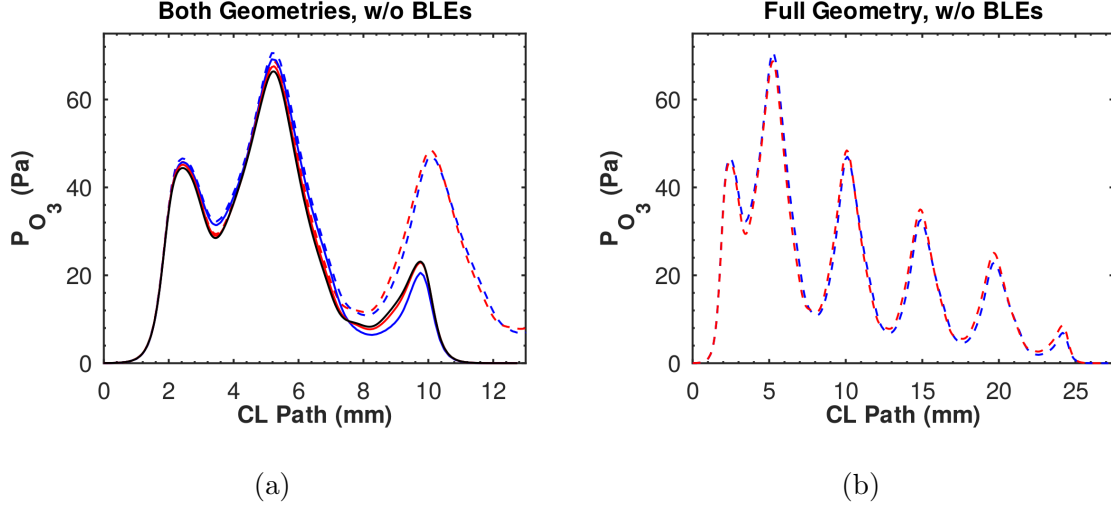


FIG. 14: Ozone partial pressure profiles, at  $Q = 350 \text{ cm}^3 \text{ min}^{-1}$ , using the no-BLEs mesh variant for selected values of  $\lambda$ : 8, 12, and 16. **(a)** Comparison between reduced (full lines) and full (dashed lines) geometries; **(b)** full view of the profile for the full geometry.

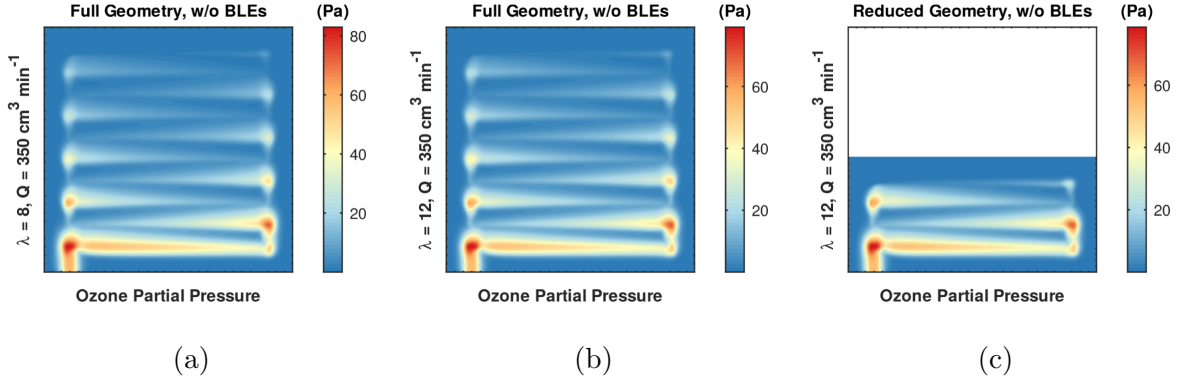


FIG. 15: Ozone partial pressure surfaces for selected values of  $\lambda$  and  $Q = 350 \text{ cm}^3 \text{ min}^{-1}$ , using the no-BLEs mesh variant: **(a)** full geometry,  $\lambda = 8$  and **(b)**  $\lambda = 12$ , and **(c)** reduced geometry,  $\lambda = 12$ .

up the possibility of further studying the numerical aspects of the model as function of the mesh, extending the current analysis to structured meshes and improved unstructured mesh schemes that may allow denser meshes with comparable computational resources.

### 3. Estimation of Discretization Error

Given the qualitative analysis of Sections III A 1 and III A 2, it might be argued that the variables chosen to track mesh convergence do not, in fact, show convergence. Not only the convergence appears to be relatively slow, some variables also show non-monotonic behavior depending on the mesh scheme. While a robust sign of convergence would be ideal, given the computational resources and accuracy of experimental data available, it is important to point out, as did Roache[17], that most of the time actual mesh convergence is impractical. Thus, instead of going further down this rabbit hole, we chose to accept the fact that the model has some error due to discretization, and tried to estimate that. We will now present the results from the generalized Richardson extrapolation (GRE), following Roache[17], and the mixed-order extrapolation (MOE), following Roy[18], used to estimate the discretization error of the scalar variables, according to Section II B 2.

First and foremost, it should be pointed out that, given the convergence behavior observed in Section III A 1 and the refinement ratios used in this study, it was not clear which set of meshes should be used in the extrapolations in order to accurately reproduce the behavior seen. It is pointed out by Roache[17] that the refinement ratio between grids,  $r$ , should be  $r > 1.3$ , in order to be able to minimize other possible numerical errors when performing the convergence study. Thus, some tests were done with the reduced geometry following this suggestion, and the following was concluded: i) the extrapolation schemes show different results depending on the mesh scheme, i.e. with or without BLEs, although the differences are relatively small and mainly concerns the region at high  $h$ ; ii) when the dataset used to calculate the extrapolate display non-monotonicity, the GRE returns complex values for the accuracy order and, consequently, to the extrapolate, although the magnitude of the imaginary term is relatively small; iii) the GRE and the MOE show different behavior according to which scalar is being analyzed, with both schemes showing similar results for the  $\Delta P/P_{\text{in}}$  only; iv) the GRE appears to converge as finer meshes are used to calculate it, in particular for the  $\Delta\chi_{\text{O}_3}/R'_{\text{O}_3}$  ratio, while the MOE appears to exaggerate the non-monotonic behavior in these cases; and v) including a third-order term in the MOE improves its results over the whole  $h$  range. The trends observed when evaluating the extrapolation schemes are likely to be related to the non-monotonicity of the data, as suggested in [18], particularly the fact that the MOE deals, in principle, with such data sets, while the GRE assumes the

data are in the asymptotic range. In these cases where the GRE returned complex values, only the real part was used to calculate the GCI. Additional information can be found in Section VI.A of the SM, while Figs. S20 and S21 show selected results of the tests done over the extrapolation schemes.

From the conclusions drawn, it was established that for the GRE the meshes to be used, for both mesh variants, were  $\lambda \in [8, 12, 16]$ , while for the MOE  $\lambda \in [2, 4, 10, 16]$  were used, with  $[4, 10, 16]$  used for the MOE up to  $h_k^2$ . The same schemes were used to estimate the discretization error on the individual variables,  $\Delta\chi_{\text{O}_3}$ ,  $R'_{\text{O}_3}$ , and  $\Delta P$ . We proceed now to evaluate the results of using the GRE and MOE schemes with the aforementioned meshes, in order to establish the best estimate of the discretization error of the reduced and full geometries of the model under study.

We start with the scalar variables already discussed in Sections III A 1 and III A 2. Figure 16 shows the scalars as function of  $h$ , with the three extrapolation schemes: GRE, 1st- and 2nd-order MOE (MOE-12), and 1st-, 2nd- and 3rd-order MOE (MOE-123). Concerning the  $\Delta\chi_{\text{O}_3}/R'_{\text{O}_3}$  ratio, Figs. 16a and 16b show that the MOEs show better agreement with the numerical results, while the GRE clearly overestimates the convergence of the variable, with very small differences between  $h = 1$  to 0. In particular, the MOE-123 shows the best fit to the entire  $h$  range, which is expected given the choice of meshes to calculate the coefficients and extrapolate. MOE-12 shows good agreement, despite the poor description at high  $h$ , in particular for the BLEs variant. However, when comparing MOE-123 to MOE-12 for the BLEs mesh variant, it appears that the derivative between  $h = 1$  and 0 is somewhat overestimated, however that is based on the assumption that for  $\lambda \geq 10$  ( $h \approx 1.5$ ) the variable is in the asymptotic range.

For the  $\Delta P/P_{\text{in}}$  ratio, Figs. 16c 16d show better agreements between the GRE and MOE schemes, however it is still clear that the GRE greatly overestimates the convergence of the variable. Like with the  $\Delta\chi_{\text{O}_3}/R'_{\text{O}_3}$  ratio, both MOE schemes show great agreement the numerical results, with MOE-12 showing relatively large differences for  $h > 3$ . Likewise, MOE-123 once again predicts an odd behavior at  $h < 1$ , in particular for the no-BLEs variant. It is not inconceivable that for  $h < 1$  a faster rate of convergence might be observed for  $\Delta P/P_{\text{in}}$ , as predicted by both GRE and MOE-123 when compared to MOE-12. However given the slow rate observed for the numerical results available, and the monotonic behavior at  $h < 4$ , it appears that the MOE-12 estimate is more plausible, particularly for the no-



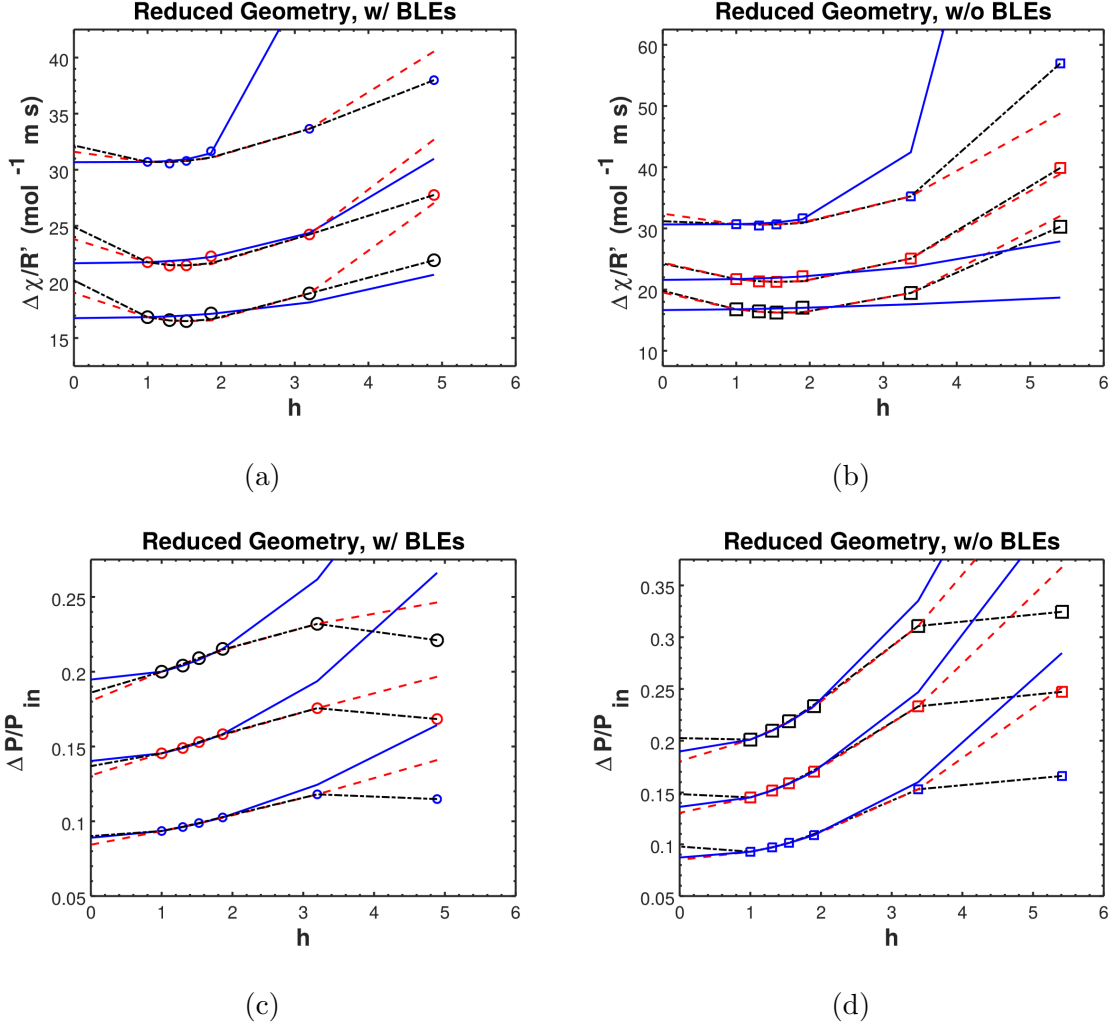


FIG. 16: Scalar variables and their respective extrapolations as functions of the normalized effective element spacing, obtained at the reduced geometry: GRE (full line), MOE-12 (dashed line), and MOE-123 (dash-dot line) (a)  $\Delta\chi_{O_3}/R'_{O_3}$  for the BLEs ( $\circ$ ) and (b) no-BLEs ( $\square$ ) mesh variants; and (c)  $\Delta P/P_{in}$  for the BLEs and (d) no-BLEs mesh variants. The following values of inlet flow rate  $Q$  are shown, with marker size increasing with  $Q$ : 250, 350 and 450 cm<sup>3</sup> min<sup>-1</sup>.

BLEs variant.

From Fig. 16, it is concluded that the MOE-12 scheme applied to the no-BLEs mesh variant provides the best agreement between extrapolation scheme and numerical results available. In addition, it was already shown that the results of both BLEs and no-BLEs mesh variants converge at low  $h$  (Fig. 4). Thus, given the smaller, albeit slightly, compu-

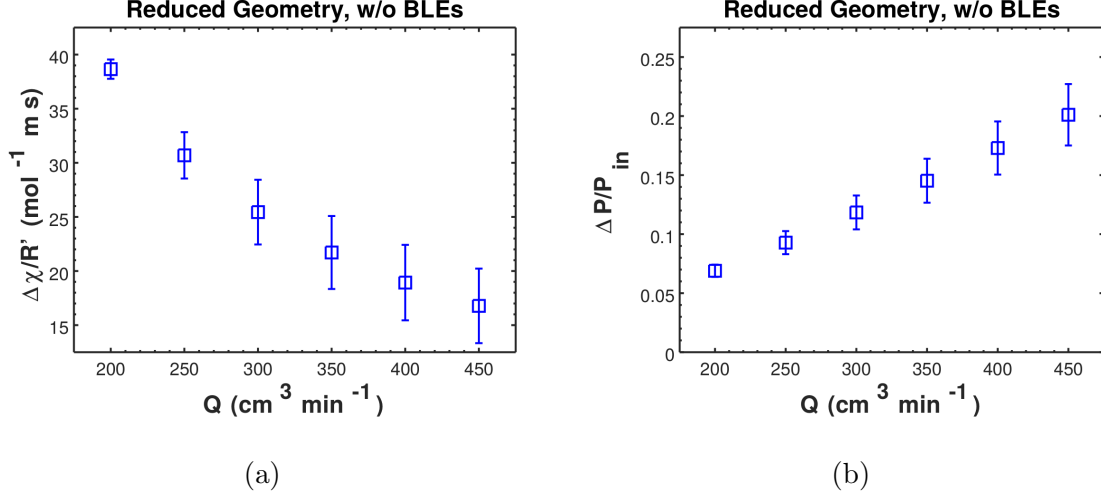


FIG. 17: Scalar variables as functions of the inlet flow rate, using the no-BLEs mesh variant with the reduced geometry: **(a)**  $\Delta\chi_{O_3}/R'_{O_3}$  and **(b)**  $\Delta P/P_{\text{in}}$ . Error bars show the estimated discretization error as given by Eq. 27.

tational cost of using the no-BLEs mesh variant, we now establish it as the standard for further studies and to estimate discretization error for the individual variables and the ratios analyzed so far. Estimation of discretization errors for the BLEs mesh variant can be found in Section VI.B of the SM (Fig. S22 and Table S9).

Carrying on, then, with the error estimate, Figure 17 shows the  $\Delta\chi_{O_3}/R'_{O_3}$  and  $\Delta P/P_{\text{in}}$  ratios as function of  $Q$ , with the estimated error bars, as given by Eq. 27. As it can be seen, the estimated error interval increases with  $Q$  for both variables, as already observed from Fig. 16. The estimated relative errors span the following intervals, with the respective averages:

$$2.31\% \leq \% \epsilon_M [\Delta\chi_{O_3}/R'_{O_3}] \leq 20.5\%, \% \bar{\epsilon}_M = 12.6\%$$

$$7.52\% \leq \% \epsilon_M [\Delta P/P_{\text{in}}] \leq 13.0\%, \% \bar{\epsilon}_M = 11.5\%$$

For the sake of completeness, and also due to experimental interest, we also briefly report the error estimate for the individual variables. Figure 18 shows the estimates for  $\Delta\chi_{O_3}$ ,  $R'_{O_3}$ , and  $\Delta P$ , as function of  $Q$ . It appears at once that the error estimates for  $\Delta\chi_{O_3}$  (Fig. 18a) are rather large. However that is only because  $\Delta\chi_{O_3}$  spans a relatively small interval for the range of  $Q$  simulated. The calculated relative error spans the interval

$$1.00\% \leq \% \epsilon_M [\Delta\chi_{O_3}] \leq 16.8\%, \% \bar{\epsilon}_M = 8.88\%,$$

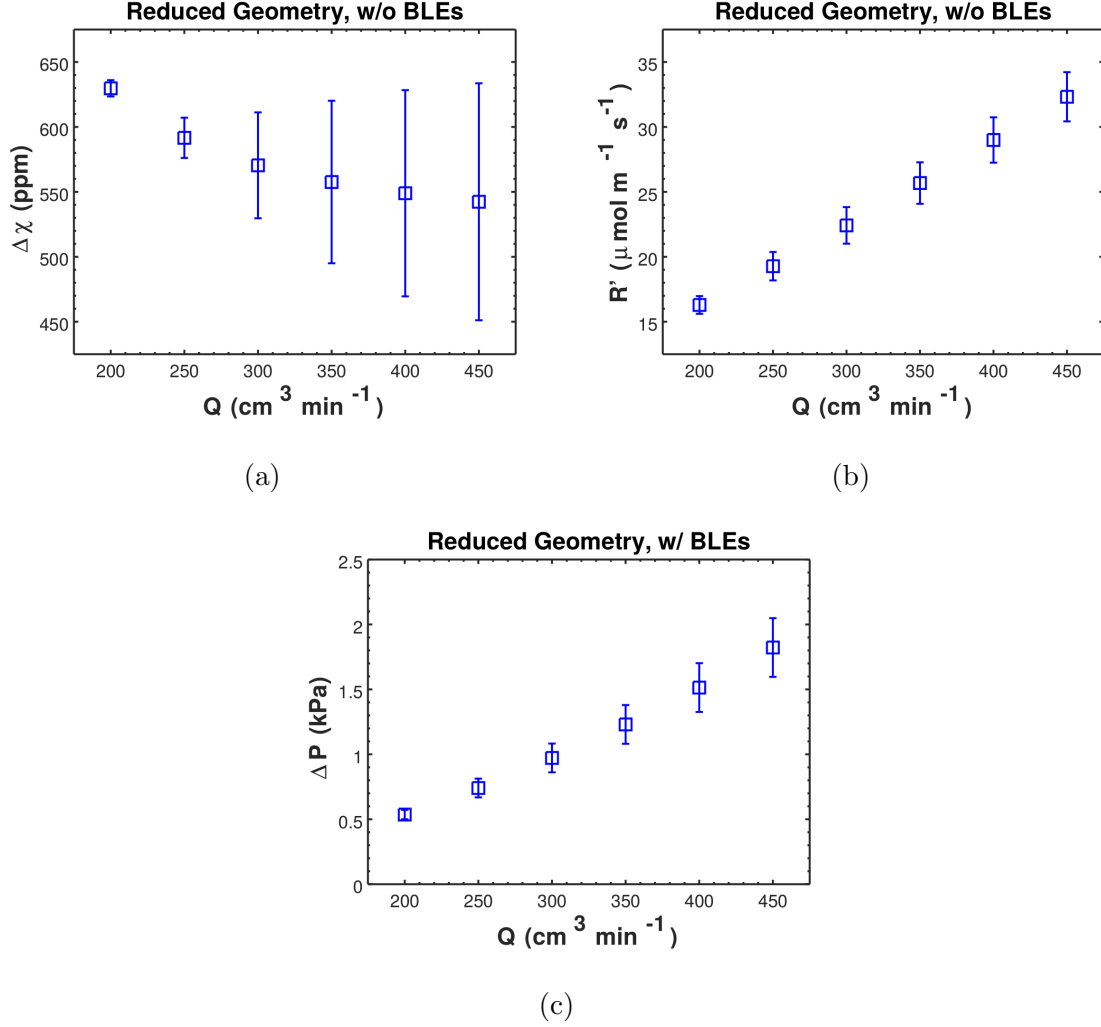


FIG. 18: Scalar variables as functions of the inlet flow rate, using the no-BLEs mesh variant with the reduced geometry: **(a)**  $\Delta\chi_{\text{O}_3}$ , **(b)**  $R'_{\text{O}_3}$ , and **(c)**  $\Delta P$ . Error bars show the estimated discretization error as given by Eq. 27.

smaller than for the  $\Delta\chi_{\text{O}_3}/R'_{\text{O}_3}$  ratio. The remaining error estimates are the following:

$$4.18\% \leq \% \epsilon_{\text{M}} [R'_{\text{O}_3}] \leq 6.28\%, \% \bar{\epsilon}_{\text{M}} = 5.70\%$$

$$6.74\% \leq \% \epsilon_{\text{M}} [\Delta P] \leq 12.4\%, \% \bar{\epsilon}_{\text{M}} = 10.8\%$$

While the magnitude of the error estimates might be one order too high, errors of  $\sim 10\%$  are not absurd, in particular considering the lower values estimated for the directly comparable scalar variables,  $\Delta\chi_{\text{O}_3}$ ,  $R'_{\text{O}_3}$ , and  $\Delta P$ . Two points should be noticed, however. First, it is once again pointed out that the goal of this work is, in part, to estimate the discretization error of the model under discussion, not to prove a point regarding its accuracy. Mathemat-

ical framework aside, these errors are in principle improvable with additional computational resources.

Secondly, these are the estimates for the reduced geometry, which allows a significantly finer mesh and, given the behavior seen in Fig. 16, should present smaller error estimates than the full geometry. Estimating the errors for the full geometry is not straightforward, however, given what is now known of the behavior of the scalar variables as functions of  $h$  and the effect different mesh schemes have on the extrapolates. Given the estimate of the exact value using the MOE-12 scheme, one may estimate the error at a given  $h$  for the reduced geometry using Eq. 27. Scaling between the reduced and full geometries might be necessary, however, as the scalar ratios used to track convergence are not entirely independent of the geometry. Fig. S23 shows that, for a good approximation, the  $\Delta\chi_{\text{O}_3}/R'_{\text{O}_3}$  and  $\Delta P/P_{\text{in}}$  ratios for the full geometry are linear functions of the ones for the reduced geometry. In particular, as can be expected from Fig. 12, the  $\Delta\chi_{\text{O}_3}/R'_{\text{O}_3}$  ratios are, to a very good approximation, related by  $f_{\text{full}} = f_{\text{reduced}} + C$ , where in this case  $C \approx 0.88$  (red line in Fig. S23). Thus, the error estimate obtained for the reduced geometry, at  $\lambda = 12$ , is a good estimate for the full geometry. For  $\Delta P/P_{\text{in}}$ ,  $f_{\text{full}} \approx 0.03 + 1.39f_{\text{reduced}}$ , thus a scaling coefficient of 1.39 should provide an estimate for the full geometry based on the reduced one, albeit not a rigorous one. Similar procedures were taken for the individual variables, where it was found that  $\Delta\chi_{\text{O}_3}$  shows a scaling coefficient of 0.954, while for  $R'_{\text{O}_3}$  it is 1.72, and for  $\Delta P$  of 1.72 (See Section VII of the SM).

With these points in mind, Figures 19 and 20 present the scalar variables of interest, respectively the ratios and individually, for the full geometry using the no-BLEs mesh variant. In Fig. 19 it can be seen that the error estimates for the ratios are quite similar for both geometries, albeit higher. This is expected given how the estimate was taken and the small differences already seen between meshes with  $\lambda = 12$  and 16 (Fig. 4). The error estimates span the intervals:

$$\begin{aligned} 2.18\% \leq \% \epsilon_{\text{M}} [\Delta\chi_{\text{O}_3}/R'_{\text{O}_3}] &\leq 22.4\%, \% \bar{\epsilon}_{\text{M}} = 13.8\% \\ 9.67\% \leq \% \epsilon_{\text{M}} [\Delta P/P_{\text{in}}] &\leq 16.1\%, \% \bar{\epsilon}_{\text{M}} = 14.0\% \end{aligned}$$

For the individual variables, Fig. 20 also shows the available experimental data, previously reported in [1]. Again the pattern follows closely that of the reduced geometry, with

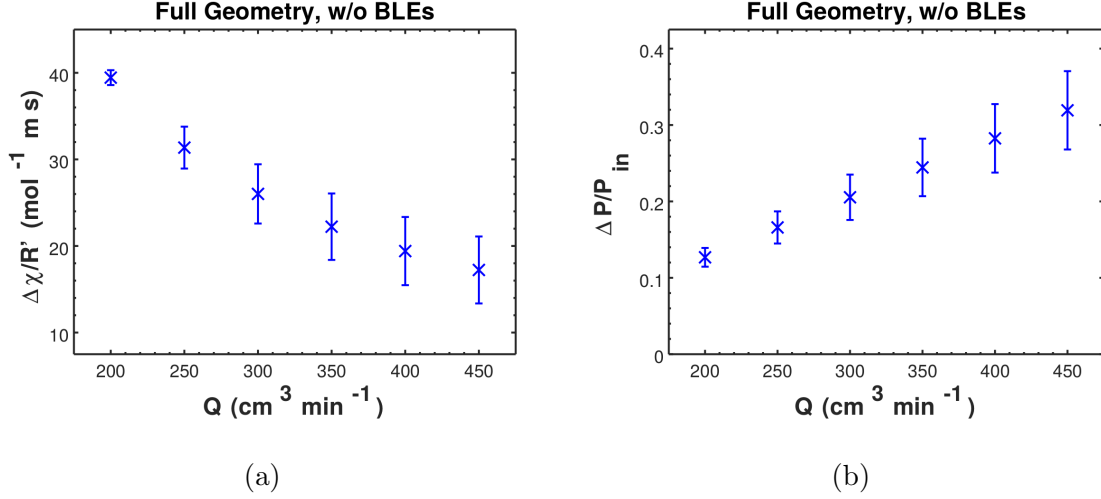


FIG. 19: Scalar variables as function of the inlet flow rate, using the no-BLEs mesh variant with the full geometry: **(a)**  $\Delta\chi_{\text{O}_3}/R'_{\text{O}_3}$  and **(b)**  $\Delta P/P_{\text{in}}$ . Error bars show the estimated discretization error as given by Eq. 27.

slightly higher error estimates. The calculated error estimates span the following intervals:

$$0.895\% \leq \% \epsilon_{\text{M}} [\Delta\chi_{\text{O}_3}] \leq 9.65\%, \% \bar{\epsilon}_{\text{M}} = 5.10\%$$

$$6.19\% \leq \% \epsilon_{\text{M}} [R'_{\text{O}_3}] \leq 8.67\%, \% \bar{\epsilon}_{\text{M}} = 7.93\%$$

$$10.9\% \leq \% \epsilon_{\text{M}} [\Delta P] \leq 17.7\%, \% \bar{\epsilon}_{\text{M}} = 15.6\%$$

with increased error estimates for  $R'_{\text{O}_3}$  and  $\Delta P$ , in line with what was presented above, and a slight reduction in maximum and average error estimates for  $\Delta\chi_{\text{O}_3}$ . This might be related to the higher absolute values of  $\Delta\chi_{\text{O}_3}$ , for the full geometry, while using a scaling similar to the reduced geometry when solving the model. Despite such fact, Fig. 20a still shows that, compared to the available experimental data, the absolute error is much greater, approximately 10 times for  $Q \geq 300 \text{ cm}^3 \text{min}^{-1}$ . For  $\Delta P$ , the situation is somewhat better, with errors showing at least the same order of magnitude. Nevertheless, it is clear that the meshes being used have great need for improvement, given the precision already available to the experimental device, and the expected increase with future developments.

We conclude this section and the grid convergence analysis of the PEFC prototype model by summarizing the results shown and discussed above. We reiterate the need to assess the uncertainty in a numerical model, be it low or not. The reduced and full geometries used to estimate the discretization error of the model show that the model has great need of

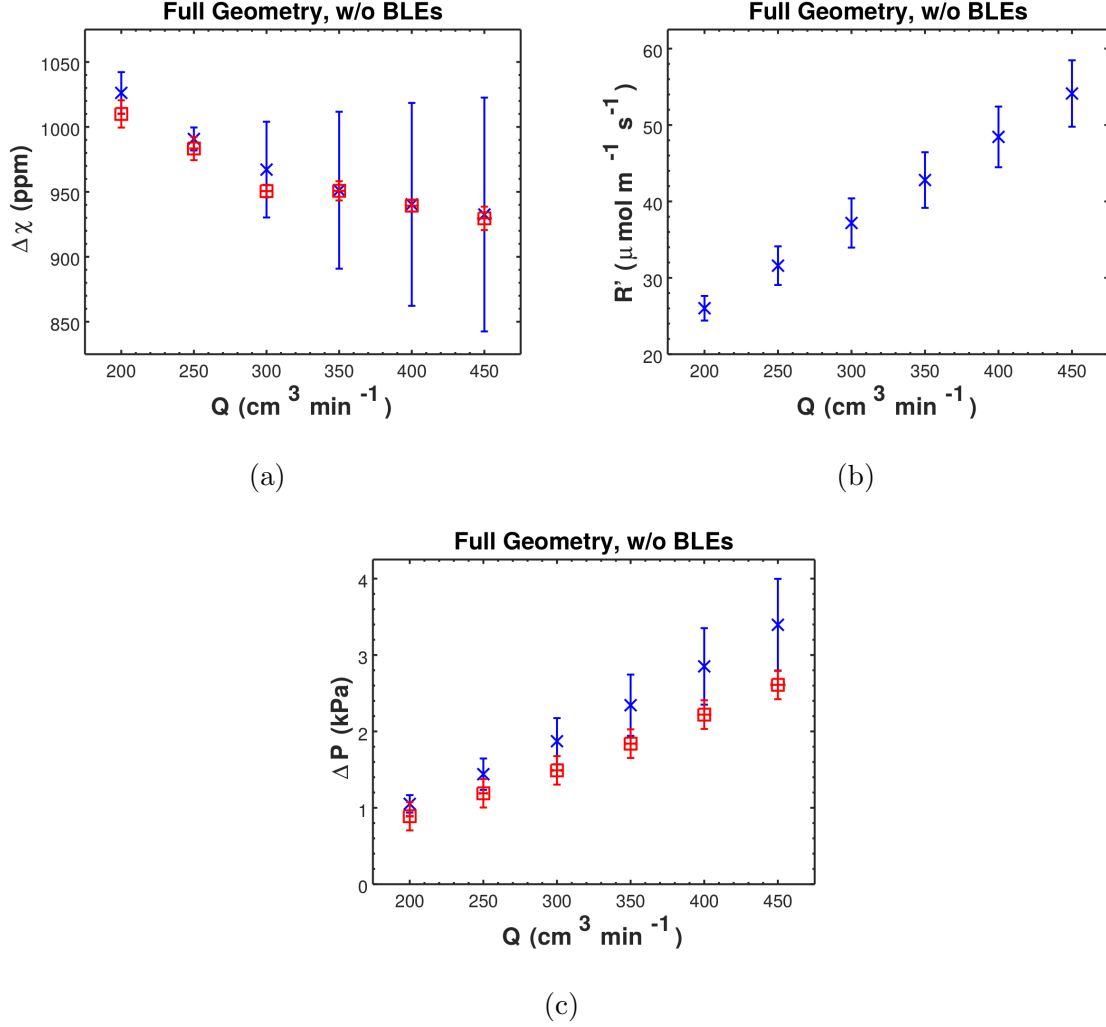


FIG. 20: Scalar variables as function of the inlet flow rate, using the no-BLEs mesh variant with the full geometry: **(a)**  $\Delta\chi_{\text{O}_3}$ , **(b)**  $R'_{\text{O}_3}$ , and **(c)**  $\Delta P$ . Shown are the numerical results ( $\times$ ) and available experimental data[1] ( $\square$ ). Error bars show the estimated discretization error as given by Eq. 27, for the numerical results, and one standard deviation for the experimental data.

mesh improvement, since the estimated relative errors, even for the best meshes, are  $\sim 10\%$  and above. However, the grid convergence analysis shows that the experimentally relevant variables, discussed overall in Section III A, show relatively slow convergence, particularly  $\Delta P$ , but also non-monotonic behavior that depends not only on the element size, but also on the mesh scheme. Thus, in addition to finer meshes and additional computational resources, it could be helpful to search for alternatives that might contribute to faster grid convergence,

such as structured grids, which might facilitate the convergence analysis, but also higher-order interpolation schemes, that, while with increased computational costs, might allow improved error estimates.

## B. Model Comparison

Having established the mesh scheme and error estimates for the reduced and full geometries, we move on to compare the improved mathematical framework, Beta, described in Section II A 2, with the already published simplified model, Alpha, described in Section II A 1 and [1]. As mentioned in Section I, the improvements were made based on well-known limitations of the original model, regarding the physical phenomena described by the model. While a better fit to experimental data is expected, it is not at all guaranteed and neither is the current goal of this work. A brief discussion will afterwards address this points along with others and further improvements that might be important for the model.

Starting with the scalar variables, both the  $\Delta\chi_{\text{O}_3}/R'_{\text{O}_3}$  ratio and the individual variables are shown in Figure 21. As mentioned in Section II C, the variables concerning the flow field are left to the SM (Section VIII.A of the SM, Figs. S24 and S25). The most straightforward comparison between models is given by the  $\Delta\chi_{\text{O}_3}/R'_{\text{O}_3}$  ratio, Fig. 21a, as it disregards the differences in reaction modeling and rate constant. It can be observed that the Beta model shows a smaller rate of variation with  $Q$  than the Alpha model, which readily demonstrates that the changes implemented significantly affect the results, and not just quantitatively. The individual variables,  $\Delta\chi_{\text{O}_3}$  and  $R'_{\text{O}_3}$  (Figs. 21b and 21c, respectively), elucidates the smaller rate seen in Fig. 21a, with the Beta model showing a slower rate of change in  $\Delta\chi_{\text{O}_3}(Q)$  as well as a slightly higher slope for  $R'_{\text{O}_3}(Q)$ . It is worth pointing out that, for  $\Delta\chi_{\text{O}_3}$ , the Beta model shows much better correlation with experimental data, although one must remember that the reaction rate constants are degrees of freedom for both formulations. Despite such freedom, Fig. 21b strongly suggests that the Alpha model, at the current mesh, is not capable of reproducing the experimental behavior with only changes in the apparent reaction rate  $k_{\text{app}}$ . In addition, it could be argued that, given the behavior of  $\Delta\chi_{\text{O}_3}$  with the grid, even in the asymptotic range would the Alpha model correlate as well as the Beta model. However, at the present moment, that is mere speculation.

It should be pointed out the difference in behavior between Alpha and Beta models for

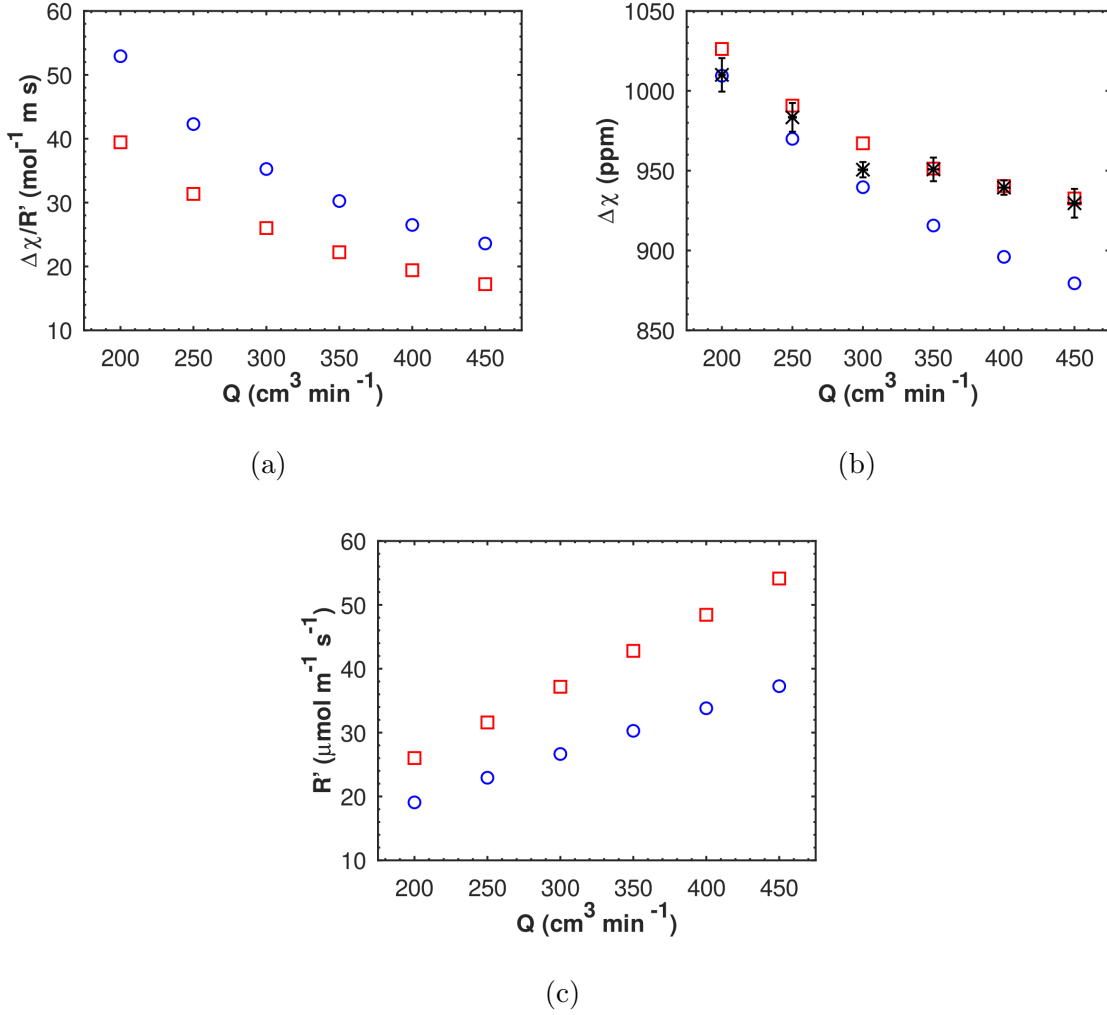


FIG. 21: Scalar variables as function of the inlet flow rate for the Alpha ( $\circ$ ) and Beta ( $\square$ ) models: **(a)**  $\Delta\chi_{\text{O}_3}/R'_{\text{O}_3}$ , **(b)**  $\Delta\chi_{\text{O}_3}$ , and **(c)**  $R'_{\text{O}_3}$ . Experimental data[1] ( $\times$ ) is also shown in **(b)** as a reference, with error bars representing one standard deviation.

$\Delta\chi_{\text{O}_3}(Q)$ . The behavior seen in Fig. 21b is in contrast to the conclusion drawn in [1]: when comparing between Stokes-Darcy (SD) and Darcy-Brinkman (DB) formulations, the latter showed a closer fit to experimental data, resembling the current Beta model; where the current Alpha model more closely resembles the SD formulation of [1]. That is a testimony of how important grid convergence studies are, as it is clear now that the correlation between experiment and the Alpha model is not as good as expected.

Returning to the comparison between the Alpha and Beta models, using the DB formulation, we move on to the  $P_{\text{O}_3}$ -related quantities. Figure 22 shows the profiles along the  $x$  axis,



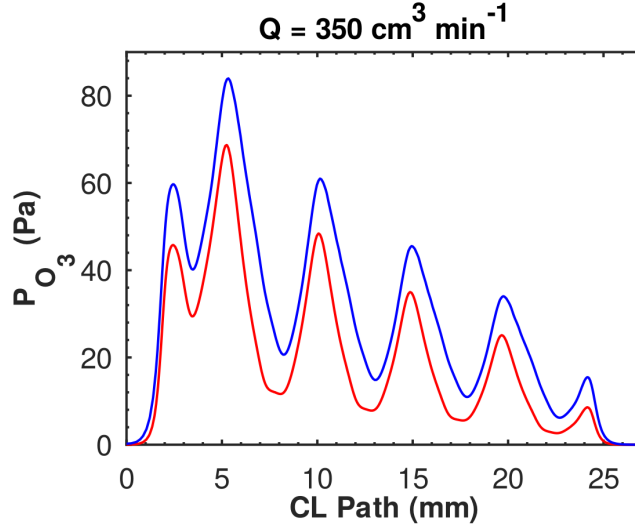


FIG. 22: Ozone partial pressure profiles, at  $Q = 350 \text{ cm}^3 \text{ min}^{-1}$ , for the Alpha (blue) and Beta (red) models.

for  $Q = 350 \text{ cm}^3 \text{ min}^{-1}$ . As expected given Fig. 21b, where the Beta model shows higher  $\Delta\chi_{\text{O}_3}(Q)$  values,  $P_{\text{O}_3}$  values for the Beta model are lower. And just like the discussion given above for the difference in  $\Delta\chi_{\text{O}_3}/R'_{\text{O}_3}$  ratio and the individual variables, this case is also not just a matter of reaction formulation and rate constant. Fig. S29 shows the same profiles normalized by their respective  $R'_{\text{O}_3}$  values. In this case, it can be seen that the difference is even larger, corroborating the idea that changes in  $P_{\text{O}_3}$  at the CL are due to more than just the different reaction kinetics. However both profiles are very similar, with small differences seen between local maxima, with the Alpha model showing a more pronounced local minima, while the Beta model shows a slightly larger region of low  $P_{\text{O}_3}$ .

For the final comparison, the  $\mathbf{P}_{\text{O}_3}$  surfaces are shown, for selected values of  $Q$ , in Figure 23. It is readily seen that Alpha shows higher  $P_{\text{O}_3}$  values than the Beta model. Aside from that, as expected from Fig. 22, there is little difference between the models. The somewhat broader local minima seen for Beta in Fig. 22 can be seen to result from lower  $P_{\text{O}_3}$  values overall, which leads to smaller ozone plumes but with no apparent additional qualitative effects. A surface of differences in  $P_{\text{O}_3}$  could be instructive, however the difference in reaction kinetics makes such data misleading, and must therefore be left out from the analysis.

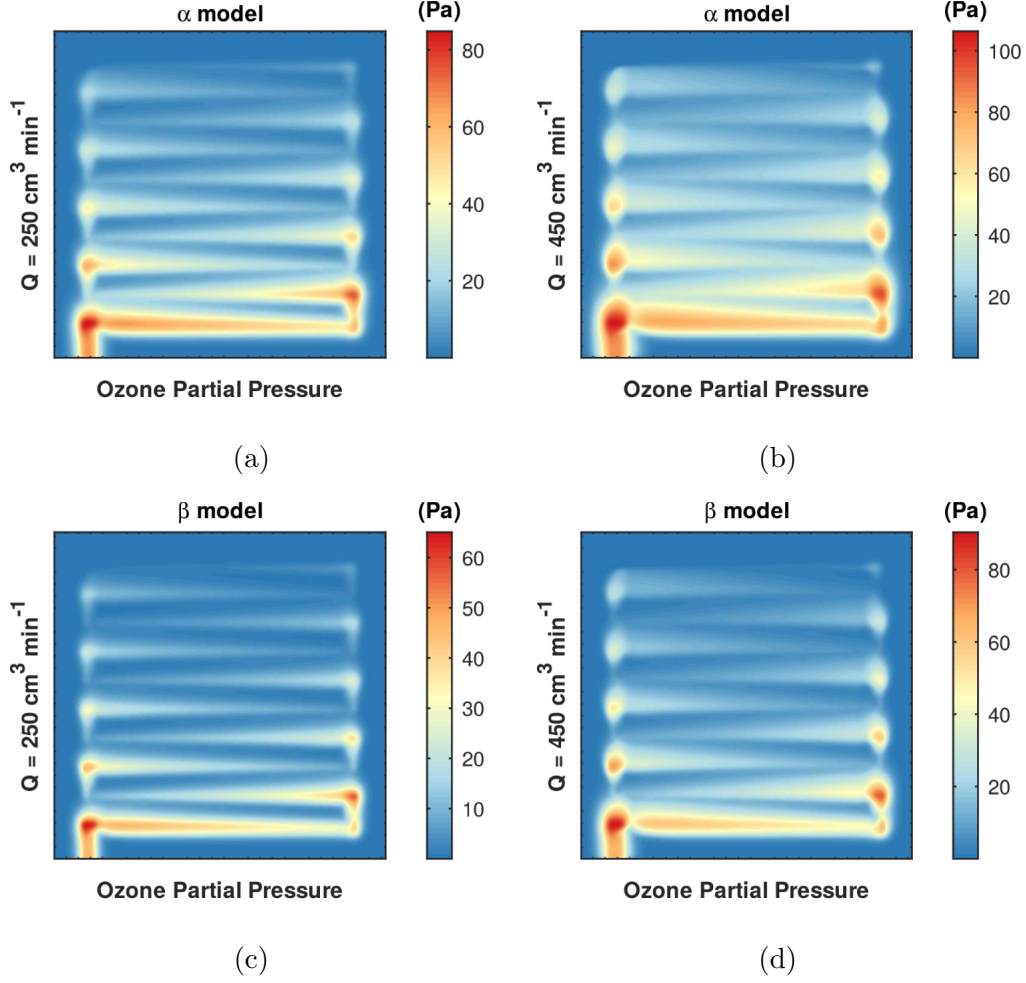


FIG. 23: Ozone partial pressure surfaces for the Alpha (top row) and Beta (bottom row) models, for  $Q = 250$  (left column) and  $450 \text{ cm}^3 \text{ min}^{-1}$  (right column).

### C. Discussions

Given the comparisons made above, it is clear that, in general, the differences between the Alpha and Beta models are relatively small, in particular with few qualitative differences. The most relevant difference seen, in Fig. 21b, lacks validation power due to the degree of freedom assigned to the reaction rate constants. To complicate matters, there is the estimated error of the Beta model, which (un)comfortably puts both experimental and Alpha model's data within uncertainty bounds (see Fig. S31), even more so if one assumes the discretization error of Alpha is of the same magnitude as Beta. Variables that show error compensation and thus would be useful for validation, such as  $\Delta\chi_{\text{O}_3}/R'_{\text{O}_3}$  and  $R'_{\text{O}_3}$  (Figs. S31a and S31d, respectively), lack experimental data. Therefore, two major issues

outside the mathematical framework need to be further considered before actual validation may be pursued: i) discretization error, i.e. the mesh refinement, and ii) the availability of experimental data. While both demand time and resources, they are currently being sought.

In the meantime, there are some shortcomings and approximations in the Beta model that deserve some clarifications. These have been brought up in Section II A 2, namely the Fickian diffusion coefficient for  $O_3$ , the use of an  $O_3$ /air mixture, and the coupling between free, porous media and Knudsen diffusion. In addition, there is the insight regarding the behavior of  $\Delta\chi_{O_3}$  when compared to the experimental data and previously published results[1]. Concerning the first point, we are not aware of the existence of measurements or calculations of the binary diffusion coefficients for ozone in any mixture. Following the rationale provided in Section II A 2, i.e. that the concentration of  $O_3$  is small and the relative concentrations of  $N_2$  and  $O_2$  are constant, and given such limitation, it seems that there is little else to be done at this moment other than directly using the single-component diffusion coefficient.

Regarding the mixture, it was mentioned in Section II A 2 that the Beta model uses a simplified formulation for the fluid’s species. As reported in [2], the experimental device used  $O_3$ -enriched air as working fluid, and thus a first approach would be to model its species as a  $O_3/O_2/N_2$  fluid. However it is known that only the  $O_3$  is reactive in the experimental conditions used, and that  $\chi_{O_3} \sim 10^{-3}$  at the inlet. Thus one might consider that  $\chi_{O_2}$  and  $\chi_{N_2}$  are approximately constant. Indeed, this is the same rationale behind the diluted species approach used previously[1]. This has two implications, namely i) the fluid’s properties, i.e. viscosity and density, are largely due to  $O_2$  and  $N_2$ , and thus very much like air; and ii) the chemical driving forces acting on  $O_3$  are mainly given by  $\nabla\chi_{O_3}$  in a bath of air. Therefore, an alternative would be to model the fluid using effective “air” molecules along with  $O_3$ . In this way, one saves computational resources while at the same time reducing the hardships of measuring, or calculating, the binary diffusion coefficients for each pair of species in the fluid at varied concentrations.

Additional simulations were carried out using the proper  $O_3/O_2/N_2$  mixture, however still using the same diffusion coefficient of Table II for  $O_3 - O_2$  and  $O_2 - N_2$  pairs. Section II of the SM provides additional information on the simulations, as well as the results (Figs. S1 to S3). While the reduced geometry was used for these simulations, they are compared against results for the  $O_3$ /air mixture using the same geometry. For all cases,

scalar variables,  $O_3$  profiles and surfaces, the differences are negligible, particularly when considering the estimated discretization errors. Notably, Fig. S3 shows the difference in  $P_{O_3}$  between mixtures, where it is shown that, while a spatial pattern is seen, suggesting a physical effect, the differences in  $O_3$  partial pressure are  $\sim 0.1$  Pa, which amounts to  $\sim 0.1\%$  of the values observed. Thus, considering both the error estimates and the order of magnitude of the experimentally relevant variables, it is safe to assert that, for the moment, the  $O_3$ /air approximation is adequate.

Concerning the coupling between diffusion modes, it was pointed out in Section II A 2 that it was not entirely clear at this point. By that it is meant the mathematical relation that expresses the effective diffusion coefficient that would be measured in a macroscopic device,  $D_i$ . Here it was chosen to apply a correction to the free diffusion coefficient, i.e. the Maxwell-Stefan binary diffusion coefficient, due to the porous media, which was then coupled to Knudsen diffusivity. This represents the understanding that, regardless of the distribution of characteristic lengths in the pore network, the sheer existence of such network and its tortuosity affects molecular diffusion, while the Knudsen regime exists alongside it. In appropriate circumstances, the Knudsen regime becomes dominant ( $Kn \sim 1$  and above,  $Kn$  being the Knudsen number), and the macroscopic description of the porous medium, using porosity and tortuosity, breaks down.

In order to assess the importance of this effect in the Beta model, additional numerical simulations were carried with the reduced geometry mentioned above and the  $O_3$ /air mixture. This was chosen, in addition to the justification presented above, as it becomes straightforward to apply different coupling schemes and to verify the contributions of each diffusion mode, given that in such case there is only one entry in the Maxwell-Stefan diffusion matrix, and thus a single generalized Fick diffusivity is calculated. Additional information can be found in Section III of the SM, and the simulations' results are shown in Figs. S4 to S7. Five settings were tested, although due to limitations of the software, only two couplings involving all processes were considered, namely the one described in Section II A 2 and one where the porous media correction is applied after coupling free and Knudsen diffusivities. The results show that the most important effect, for the simulated device, is the porous media correction. This is in line with previous work[1], where it was argued that the low Knudsen numbers ( $Kn \sim 10^{-3} - 10^{-2}$ ) calculated for the device implied small contributions from Knudsen diffusion. Indeed, Fig. S7 shows the differences in  $P_{O_3}$  between the

chosen coupling, Eq. 11, and the other four settings, where again a spatial pattern and larger partial pressure difference are seen when the alternative setting lacks porous media corrections. The differences due to a lack of Knudsen diffusion are of the same order as the difference between both settings including all effects ( $\Delta P_{\text{O}_3} \sim 0.01$  Pa), however showing a noisy spatial pattern, while the latter shows a clear pattern. Considering the anecdotes reported in [1], concerning differences between concentrated and diluted species approaches, these results suggest that concentration and pressure gradients, considered in the Maxwell-Stefan formulation, are also more important than Knudsen diffusion for the experimental device under consideration.

Finally, a brief discussion on the difference in behavior between Alpha and Beta models for  $\Delta\chi_{\text{O}_3}(Q)$ . As pointed out in Section IIIB, the behavior of the Alpha model resembles the one using the Stokes-Darcy formulation in [1], while the Beta model resembles the one for the Darcy-Brinkman formulation. To be clear, in this work both Alpha and Beta models use the DB formulation for free and porous media flow. This raises the question if, given the new mathematical formulation, mesh and solver schemes, the DB is actually superior to the SD formulation as previously claimed.

This was of course investigated, and it is given in Section IV of the SM, with results shown in Figs. S27 to S30. Briefly, it is seen that, for the current mesh, the fluid flow formulation affects the Alpha and Beta model differently, with most differences being solely quantitative. For instance, for a given reaction rate constant, the  $\Delta\chi_{\text{O}_3}/R'_{\text{O}_3}$  ratio reduces slightly for both models (Fig. S27a), while the  $\Delta P/P_{\text{in}}$  ratio increases for the Alpha and reduces for the Beta model (Fig. S27b). The most notable differences lies in  $\Delta\chi_{\text{O}_3}$  and  $U$   $z$ -profiles in the Pm domains. In the case of  $\Delta\chi_{\text{O}_3}$  (Fig. S27c), the Beta model shows only a quantitative change, with higher values for the same  $k_2$ . For the Alpha model, however, there is a noticeable change in slope, with higher values at small  $Q$  and lower values at high  $Q$ . This somewhat corroborates the differences seen and discussed in [1], that the SD formulation is least likely to properly fit the experimental data by just adjusting  $k_{\text{app}}$ . Concerning the  $U$   $z$ -profiles in the Pm domains, (Fig. S28), there is a significant mismatch between the SD and DB formulations. A comparison with Figure 5 of [1] will not only show a much better-resolved  $U$  profile, for all frameworks, but also closer  $U$  values between formulations. The discrepancy lies in the discontinuities in  $U$ , already noted in [1], not only between the Ch and MPS domains, but also between the MPS and CL domains. The

boundary conditions involved in both the coupling between Ch and MPS domains and the upper CL surface are knowingly different[4, 20, 22], and given deeper scrutiny might be improved or even reconciled. The  $U$  jump between different materials, however, is unlikely to be a proper description of reality, or an artifact due to a coarse mesh, as there is evidence of proper continuity in  $U$  when using Darcy’s law (see for instance [21]). Thus, this is interpreted as evidence that the SD formulation, as it has been applied, provides a poorer description of coupled free and porous media flow than the DB formulation.

Despite the advances achieved in the Beta model, in addition to the issues discussed above there are points that demand further improvements in the mathematical formulation. A Gamma model would need to consider the anisotropy and inhomogeneity of porous media, as well as solve the conundrum involving Knudsen diffusivity. Ideally, in order to further reduce the gap between the prototype PEFC and an actual device, heat transport should also be considered, as well as two-phase flow. That would demand modifications in the experimental setup, as well as additional data on the properties of the materials and species involved. Moving away from phenomena under broad scrutiny, there is a discrepancy between ozone plume sizes to solve (see also [1]). In this case, two hypothesis are currently under consideration, i) inhomogeneous mechanical deformation of the MPS, and ii) molecular slip velocities. The first stems from the way PEFC devices are usually sealed, using screws distributed around the core of the device, while the second is the breakdown of the no-slip boundary condition, which asserts that  $\mathbf{u} = 0$  at the interface between solid and fluid. It appears that, anecdotally, both are known to play a role in PEFCs, and some work has been done on both for different reasons (see [23–26] as well as [27] and references therein; and [28–31], respectively). How important would they be in actual fuel cells, however, appears little understood, as the complexity of including non-linear solid mechanics and the molecular interplay between fluid and solid species in already hard-to-solve differential equations is likely a powerful factor stymieing such research. Nevertheless, until it is done and calculated, one can only speculate.

#### IV. SUMMARY

A report is presented concerning progress on the numerical modeling of a prototype PEFC[2], building on previously published work[1]. Known limitations of the original model,

Alpha, were addressed in order to increase fidelity with the current understanding of fuel cell devices, resulting in the Beta model. In addition to the comparison between mathematical frameworks, a grid convergence study was carried out in order to provide an estimate to the discretization error intrinsic to the updated model.

Grid convergence study was carried out with two mesh schemes, differing only by the existence of so-called “boundary layer” elements (BLEs). Four variables were tracked in this study, namely the ratio between the drop in reactant molar fraction and the apparent reaction rate,  $\Delta\chi_{\text{O}_3}/R'_{\text{O}_3}$ ; the ratio between pressure drop and inlet pressure,  $\Delta P/P_{\text{in}}$ ; flow speed profiles,  $U$ ; and reactant partial pressure profiles,  $P_{\text{O}_3}$ . Convergence was assessed qualitatively using plots of the variables as a function of an effective, normalized element spacing  $h$ , and quantitatively by estimating the discretization error through continuum extrapolates using two different extrapolation schemes[17, 18]. Afterwards, given a choice of mesh scheme and estimates of discretization error, model comparison was carried out using the same mesh with both models, comparing results related to species distribution and reaction formulation, namely the  $\Delta\chi_{\text{O}_3}/R'_{\text{O}_3}$  ratio and its individual variables, the  $P_{\text{O}_3}$  profiles, and reactant partial pressure surfaces,  $\mathbf{P}_{\text{O}_3}$ .

A qualitative assessment of the grid convergence study showed that the use of BLEs leads to non-monotonic behavior in some variables, notably the  $\Delta P/P_{\text{in}}$  ratio, while the  $\Delta\chi_{\text{O}_3}/R'_{\text{O}_3}$  ratio shows non-monotonic behavior for both mesh schemes. Despite such differences at large  $h$  (i.e. coarse grids), the mesh schemes converged at low  $h$ , suggesting the results were truly approaching mesh independence. In this way, it was established that the no-BLEs mesh scheme was to be used for further assessments and in future studies, and that the finest mesh available was to be used. Prior to the quantitative assessment, analysis suggested that the so-called Mixed 1st and 2nd order extrapolation scheme[18] (MOE-12) provided the best estimate for the continuum extrapolate, possibly due to the non-monotonic behavior shown by the scalar variables analyzed. Thus, using MOE-12 on a proxy geometry (fewer channel turns), the estimates of the discretization error, in the inlet flow rate range of  $200 \leq Q \leq 450 \text{ cm}^3 \text{ min}^{-1}$ , returned average errors of 13.8% for the  $\Delta\chi_{\text{O}_3}/R'_{\text{O}_3}$  ratio (range of 2.18% to 22.4%) and of 14.0% for the  $\Delta P/P_{\text{in}}$  ratio (range of 9.67% to 16.1%).

The grid convergence study also allowed the corroboration of previously established points[1], such as the importance of the turns of the Ch domain on the global flow field, as well as the contribution of convective transport in total molar flux to, and in the Pm

domains. It was found that secondary flows in the corners of the Ch domain are quite mesh-sensitive, particularly the ones caused by boundary-layer separation (BLS). At low  $h$ , BLS produces a pronounced effect on the flow field along the straight sections of the Ch domain, deforming the  $U$  profile up to the point that, at  $Q = 450 \text{ cm}^3 \text{ min}^{-1}$ , the profile is asymmetric with respect to wall distance into the next corner, i.e. it appears that the flow does not fully develop along the straight section. Concerning reactant molar flux, integrated  $z$ -component of the molar flux at the Ch-MPS and MPS-CL boundaries corroborate a significant contribution of convection to reactant influx to the Pm domains, while average molar flux magnitude inside the Pm domains shows dominance of convective over diffusive transport. Increased mesh resolution ( $h \rightarrow 0$ ) was seen to reduce convective contribution, while simultaneously increasing diffusive transport, although both remain at similar magnitude.

Overall it must be pointed out that the model is not considered to have converged with respect to the discretization. Relative errors of order  $\sim 10\%$  in the numerical data are larger than the experimental ones available, which makes actual model validation impossible at the moment. Adding other common sources of uncertainty, such as in parameterization, it is clear that there is a need for denser meshes and schemes with faster convergence, as well as improved methods for error estimation, in the fuel cell modeling community. Given the non-monotonic behavior of some variables of experimental relevance, this work calls for increased caution when comparing numerical to experimental data and when making predictions. On the other hand, uncertainty is only problematic if not acknowledged, and we are of the opinion that a major part of modeling is knowing its limitations and uncertainties. In this way, the use of proxy models and simpler systems may be particularly useful to advance research in complex devices, such as actual fuel cells.

Concerning model comparison, relatively small differences are seen between the Alpha and Beta models. One noteworthy, qualitative difference lies in  $\Delta\chi_{\text{O}_3}$ , that shows a much better fit of the Beta model's data to available experimental data[1]. Shortcomings of the Beta model are discussed, namely the use of Fick diffusivity for  $\text{O}_3$  despite the Maxwell-Stefan formulation, the use of an approximated  $\text{O}_3$ /air mixture, and the coupling between free, porous media and Knudsen diffusion. While for the Fick diffusion coefficient there is little to be done about at the moment, the mixture and coupling between diffusion modes were investigated. It is shown that there is a negligible difference, considering the error



estimates and order of magnitude of the experimental data, between the approximate  $O_3$ /air and the proper  $O_3/O_2/N_2$  mixtures. The different coupling between diffusion modes also show negligible differences, however it is shown that the main factor affecting results is the presence of porous media correction, while the Knudsen regime appears to be of little significance for the current device.

An apparent divergence from earlier results was also addressed, where the Alpha model, at the current mesh and solver schemes, differ from previously published results[1]. New results using the Stokes-Darcy (SD) and Darcy-Brinkman (DB) formulations, with both Alpha and Beta models, show similarities between formulations for a given model, however each model is affected differently. Given the changes in  $\Delta\chi_{O_3}$ , when compared to the available experimental data, the Alpha model still shows poorer fit to the experimental data. On the other hand, flow speed profiles along the thickness of the domains show a smoother flow field for the DB formulation in both models. Thus, it is reasserted that, for the prototype PEFC device under consideration, the Beta model using the DB formulation provides a better description of the experimental data available.

It should be noted, however, that given the estimated error of the numerical data, the results shown lack validation power, as both models, and experimental data, are well within error bounds of each other. Adding uncertainties in parameterization, these results call for additional experimental data and denser meshes (i.e. more computational resources) in order to be able to accurately distinguish between models, providing further insight into the physical phenomena underlying PEFC devices. Such improvements would guide a future Gamma model as whether to include additional features, such as solid mechanics, improved porous media description and fluid flow formulations; in order to settle existing questions and, thus, further reduce the gap between experimental and computational results. Given the relatively simplicity of the model and similarity to actual PEFC devices, we believe there is much to be gained from further refining this coupled experimental-numerical approach to fuel cell research.

## ACKNOWLEDGMENTS

O.B. acknowledges the Fundação de Apoio à Universidade de São Paulo, FUSP, grant #2968. I.K and T.L. acknowledges the Fundação de Ampara à Pesquisa do Estado de

São Paulo, FAPESP, grants #2014/22130-6 and #2017/15304-6, respectively. Authors also acknowledge the Research Centre for Gas Innovation, RCGI, sponsored by FAPESP grant #2014/50279-4.[32]

---

- [1] O. Beruski, T. Lopes, A. R. Kucernak, and J. Perez. Investigation of convective transport in the so-called “gas diffusion layer” used in polymer electrolyte fuel cell. *Phys. Rev. Fluids*, 2:103501, 2017.
- [2] T. Lopes, M. Ho, B. K. Kakati, and A. R. J. Kucernak. Assessing the performance of reactant transport layers and flow fields towards oxygen transport: A new imaging method based on chemiluminescence. *Journal of Power Sources*, 274:382–392, 2015.
- [3] John W. Eaton, David Bateman, Søren Hauberg, and Rik Wehbring. *GNU Octave version 4.2.1 manual: a high-level interactive language for numerical computations*, 2017.
- [4] M. Le Bars and M. G. Worster. Interfacial conditions between pure fluid and a porous medium: implications for binary alloy solidification. *Journal of Fluid Mechanics*, 550:149–173, 2006.
- [5] R. J. Millington and J. P. Quirk. Permeability of porous solids. *Transactions of the Faraday Society*, 57:1200–1207, 1961.
- [6] Z. Fishman, J. Hinebaugh, and A. Bazylak. Microscale tomography investigations of heterogeneous porosity distributions of pemfc gdl. *Journal of the Electrochemical Society*, 157:B1643–B1650, 2010.
- [7] Z. Fishman and A. Bazylak. Heterogeneous through-plane distributions of tortuosity, effective diffusivity, and permeability for pemfc gdl. *Journal of the Electrochemical Society*, 158:B247–B252, 2011.
- [8] R. Ono and T. Oda. Spatial distribution of ozone density in pulsed corona discharges observed by two-dimensional laser absorption method. *Journal of Physics D: Applied Physics*, 37:730–735, 2004.
- [9] W. J. Massman. A review of the molecular diffusivities of H<sub>2</sub>O, CO<sub>2</sub>, CH<sub>4</sub>, CO, O<sub>3</sub>, SO<sub>2</sub>, NH<sub>3</sub>, N<sub>2</sub>O, NO and NO<sub>2</sub> in air, O<sub>2</sub> and N<sub>2</sub> near STP. *Atmospheric Environment*, 32:1111–1127, 1998.
- [10] O. Schenk and K. Gärtner. *Parallel Sparse Direct Solver PARDISO - User Guide*, versão 5.0.0 edition, 2014.

- [11] A. Picard, R. S. Davis, M. Gläser, and K. Fujii. Revised formula for the density of moist air (CIPM-2007). *Metrologia*, 45:149–155, 2008.
- [12] Supplemental Material is available at <https://arxiv.org/abs/2002.04519>.
- [13] P. R. Amestoy, I. S. Duff, J. Koster, and J.-Y. L’Excellent. A fully asynchronous multi-frontal solver using distributed dynamic scheduling. *SIAM Journal on Matrix Analysis and Applications*, 23(1):15–41, 2001.
- [14] P. R. Amestoy, A. Guermouche, J.-Y. L’Excellent, and S. Pralet. Hybrid scheduling for the parallel solution of linear systems. *Parallel Computing*, 32(2):136–156, 2006.
- [15] Y. Saad and M. H. Schultz. GMRES: A generalized minimal residual algorithm for solving nonsymmetric linear systems. *SIAM Journal on Scientific and Statistical Computing*, 7:856–869, 1986.
- [16] A. Toselli and O. B. Widlund. *Domain Decomposition Methods*. Springer, Berlin, Heidelberg, 1 edition, 2005.
- [17] P. J. Roache. Quantification of uncertainty in computational fluid dynamics. *Annu. Rev. Fluid. Mech.*, 29:123–160, 1997.
- [18] C. J Roy. Grid convergence error analysis for mixed-order numerical schemes. *AIAA J.*, 41:595–604, 2003.
- [19] The set of linear equations was solved using the *linsolve* function of Octave, without any additional options.
- [20] J. A. Ochoa-Tapia and S. Whitaker. Momentum transfer at the boundary between a porous medium and a homogeneous fluid–I. Theoretical development. *International Journal of Heat and Mass Transfer*, 38:2635–2646, 1995.
- [21] Y. Ye, G. Chiogna, O. A. Cirpka, P. Grathwohl, and M. Rolle. Experimental evidence of helical flow in porous media.
- [22] J. A. Ochoa-Tapia and S. Whitaker. Momentum transfer at the boundary between a porous medium and a homogeneous fluid–II. Comparison with experiment. *International Journal of Heat and Mass Transfer*, 38:2647–2655, 1995.
- [23] I. Nitta, T. Hottinen, O. Himanen, and M. Mikkola. Inhomogeneous compression of PEMFC gas diffusion layer. Part I. Experimental. *Journal of Power Sources*, 171:26–36, 2007.
- [24] J. Kleemann, F. Finsterwalder, and W. Tillmetz. Characterisation of mechanical behaviour and coupled electrical properties of polymer electrolyte membrane fuel cell gas diffusion layers.

- Journal of Power Sources*, 190:92–102, 2009.
- [25] A. El-kharouf, D. J. L. Mason, T. J. nd Brett, and B. G. Pollet. *Ex-situ* characterisation of gas diffusion layers for proton exchange membrane fuel cells. *Journal of Power Sources*, 218:393–404, 2012.
  - [26] S. Bakhshian and M. Sahimi. Computer simulation of the effect of deformation on the morphology and flow properties of porous media. *Phys. Rev. E.*, 94:042903, 2016.
  - [27] J. Millichamp, T. J. Mason, T. P. Neville, N. Rajalakshmi, R. Jervis, P. R. Shearing, and D. J. L. Brett. Mechanism and effects of mechanical compression and dimensional change in polymer electrolyte fuel cells - A review. *J. Power Sources*, 284:305–320, 2015.
  - [28] N. V. Priezjev, A. A. Darhuber, and S. M. Troian. Slip behavior in liquid films on surfaces of patterned wettability: Comparison between continuum and molecular dynamics simulations. *Phys. Rev. E*, 71:041608, 2005.
  - [29] T. Qian, X.-P. Wang, and P. Sheng. Hydrodynamic slip boundary condition at chemically patterned surfaces: A continuum deduction from molecular dynamics. *Phys. Rev. E*, 72:022501, 2005.
  - [30] L. Wu. A slip model for rarified gas flows at arbitrary knudsen number. *Appl. Phys. Lett.*, 93:253103, 2008.
  - [31] T. A. Ho, D. V. Papavassiliou, and A. Striolo. Liquid water can slip on a hydrophilic surface. *Proc. Natl. Acad. Sci. USA*, 108:16170, 2011.
  - [32] Author contributions: O.B. designed and conducted the research, analyzed the data and wrote the paper. I.K. and T.L. contributed with discussions and by revising the paper. T.L. and F.C.F contributed with funding sources.